Molecular Cell

Article

Mechanism of cotranslational protein N-myristoylation in human cells

Graphical abstract

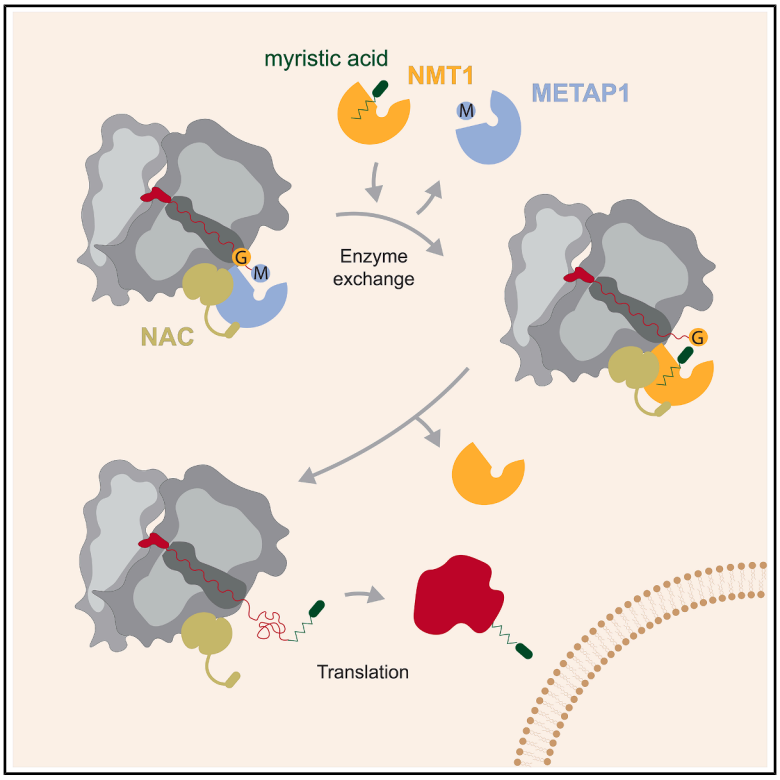

Highlights

- NAC recruits N-myristoyltransferases (NMTs) to translating ribosomes
- N-terminal methionine excision unmasks NMT motifs in nascent chains
- Structure-function analysis reveals molecular interplay of NMTs, METAP1 and NatA

Authors

Martin Gamerdinger, Blanca Echeverria, Alfred M. Lentzsch, ..., Shu-ou Shan, Nenad Ban, Elke Deuerling

Correspondence

martin.gamerdinger@uni-konstanz.de (M.G.), sshan@caltech.edu (S.-o.S.), ban@mol.biol.ethz.ch (N.B.), elke.deuerling@uni-konstanz.de (E.D.)

In brief

In structure-function studies, Gamerdinger and Echeverria et al. uncover the cotranslational mechanism of N-myristoyltransferases (NMTs), essential enzymes that attach a lipid anchor to newborn proteins. They show that NMT activity is orchestrated by a key regulator at the ribosomal tunnel exit, the nascent polypeptide-associated complex (NAC).

Gamerdinger et al., 2025, Molecular Cell *85*, 2749–2758
July 17, 2025
https://doi.org/10.1016/j.molcel.2025.06.015

CellPress

Molecular Cell

CellPress
OPEN ACCESS

Article

Mechanism of cotranslational protein N-myristoylation in human cells

Martin Gamerdinger,[1,6,*] Blanca Echeverria,[2,6] Alfred M. Lentzsch,[3,4] Nicolas Burg,[1] Ziyi Fan,[3] Mateusz Jaskolowski,[2,5] Alain Scaiola,[2] Selina Piening,[1] Shu-ou Shan,[3,*] Nenad Ban,[2,*] and Elke Deuerling[1,7,*]

[1]Department of Biology, Molecular Microbiology, University of Konstanz, 78457 Konstanz, Germany
[2]Department of Biology, Institute of Molecular Biology and Biophysics, ETH Zurich, 8093 Zurich, Switzerland
[3]Division of Chemistry and Chemical Engineering, California Institute of Technology, Pasadena, CA 91125, USA
[4]Present address: Department of Molecular Biology and Genetics, Johns Hopkins University School of Medicine, Baltimore, MD 21205, USA
[5]Present address: Department of Pharmacology, University of Cambridge, Cambridge CB2 1PD, UK
[6]These authors contributed equally
[7]Lead contact
*Correspondence: martin.gamerdinger@uni-konstanz.de (M.G.), sshan@caltech.edu (S.-o.S.), ban@mol.biol.ethz.ch (N.B.), elke.deuerling@uni-konstanz.de (E.D.)
https://doi.org/10.1016/j.molcel.2025.06.015

SUMMARY

N-myristoyltransferases (NMTs) cotranslationally transfer the fatty acid myristic acid to the N terminus of newly synthesized proteins, regulating their function and cellular localization. These enzymes are important drug targets for the treatment of cancer and viral infections. N-myristoylation of nascent proteins occurs specifically on N-terminal glycine residues after the excision of the initiator methionine by methionine aminopeptidases (METAPs). How NMTs interact with ribosomes and gain timely and specific access to their substrates remains unknown. Here, we show that human NMT1 exchanges with METAP1 at the ribosomal tunnel exit to form an active cotranslational complex together with the nascent polypeptide-associated complex (NAC). NMT1 binding is sequence selective and specifically triggered by methionine excision, which exposes the N-myristoylation motif in the nascent chain. The revealed mode of interaction of NMT1 with NAC and the methionine-cleaved nascent protein elucidates how a specific subset of proteins can be efficiently N-myristoylated in human cells.

INTRODUCTION

The correct cotranslational N-terminal modification of newly synthesized proteins is a central cellular process that ensures the stability, function, and localization of proteins.[1–3] In eukaryotes, a large fraction of proteins requires two sequential enzymatic modifications: the removal of the N-terminal initiator methionine through methionine aminopeptidases (METAPs), followed by acetylation of the neo-N terminus by N-acetyltransferase A (NatA) or lipidation by N-myristoyltransferases (NMTs).[1–5] METAPs have a large substrate pool (>40% of all cytosolic proteins) encompassing virtually all proteins with a small and uncharged amino acid at the second position (G, A, C, V, S, T, or P).[6,7] After methionine excision, most of these substrates are acetylated by NatA.[1,2,4] These include many substrates with a glycine residue at the neo-N terminus, with the exception of a small subset of proteins that require lipidation by NMTs.[8–10]

NMTs are highly conserved and essential enzymes that transfer myristic acid, a 14-carbon saturated fatty acid, from the donor myristoyl-Coenzyme A (myr-CoA) to the free α-amino group of glycine residues of specific target proteins (>500 different substrates in human cells).[8–10] In certain substrates, NMTs can also myristoylate the ε-amino groups of lysine side chains.[11,12] NMT substrates share a characteristic N-terminal consensus sequence, MGxxxS (x = variable but with preference/exclusion of certain amino acids; see Castrec et al.[8]), and often have a positively charged residue at position 7.[8–10,13,14] The hydrophobic lipid modification critically influences the function and cellular localization of NMT target proteins by regulating their interactions with cell membranes. N-myristoylation of proteins by NMTs plays a key role in multiple biological processes important for oncology, virology, and immune function. The two closely related human NMT paralogs, NMT1 and NMT2,[12,14] are proven drug targets and the subject of several current clinical trials for the treatment of cancer and viral infections.[15–19] The cotranslational mechanisms of action of these enzymes remain poorly understood.

Recent studies have revealed that cotranslational N-terminal methionine excision and acetylation are physically coupled processes mediated by the nascent polypeptide-associated complex (NAC), a ubiquitous heterodimeric (NACα/NACA + NACβ/BTF3b) ribosome-associated protein biogenesis factor.[2,20,21]

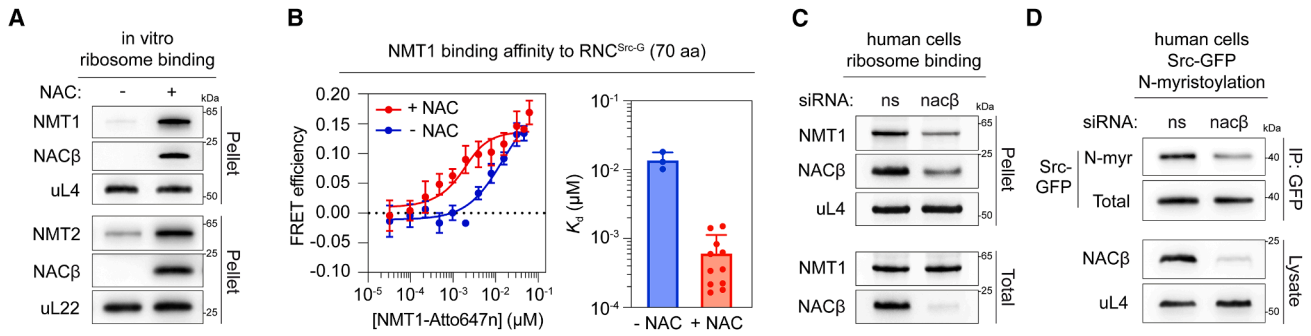

Figure 1. NAC recruits NMTs to translating ribosomes

(A) Co-sedimentation of human NMT1 and NMT2 with ribosomes *in vitro* in the presence and absence of NAC. Ribosomal pellet fractions were analyzed by immunoblotting.

(B) Equilibrium titrations to measure the binding affinity of NMT1 for RNC$^{Src\text{-}G}$ in the presence and absence of NAC (left). Binding was measured based on FRET between Cy3B (donor) labeled at position 28 in the Src nascent chain and Atto647N (acceptor) labeled on NMT1. The data are shown as mean ± SD (n = 3 for the −NAC sample and n = 9 for the +NAC sample) and were fit to Equation 3. The obtained K_d values are summarized on the right, showing the values from independent titrations and in Table S1.

(C) Ribosome association of NMT1 after knockdown of NACβ in human HEK293T cells. Proteins in total and ribosomal pellet fractions were detected by immunoblotting.

(D) N-myristoylation of the NMT model substrate (Src N terminus fused to GFP) after knockdown of NACβ in human HEK293T cells. Protein levels were detected by immunoblotting.

See also Figure S1 and Table S1.

NAC recruits both required enzymes, METAP1 and NatA, simultaneously to the ribosome tunnel exit using two different flexible tails, resulting in the formation of a cotranslational multienzyme complex that ensures the efficient two-step modification of nascent proteins.[20,21] However, NMTs also need to gain access to nascent chains after methionine excision, and NMTs must engage their specific substrates before NatA to prevent their potential acetylation by this competing enzyme, which also targets N-terminal glycine residues.[8,22] How NMTs interact with the ribosome and how their binding is spatiotemporally regulated relative to METAP1 and NatA to ensure efficient and specific N-myristoylation of nascent proteins is unknown. In this study, we elucidate the cotranslational mechanism of action of human NMTs and their interplay with NAC, METAP1, and NatA.

RESULTS

NAC recruits NMTs to translating ribosomes

We sought to identify factors that regulate the binding of human NMTs to translating ribosomes. NMTs must act on nascent proteins directly after the removal of the initiator methionine by METAPs. Since NAC facilitates the binding of METAP1 to translating ribosomes,[20,21] a functional interaction between NAC and NMTs is conceivable. To investigate this possibility, we performed ribosome binding studies *in vitro* using purified human NAC and NMT1. NMT1 alone bound only weakly to ribosomes, whereas the addition of NAC strongly enhanced the ribosome interaction of the enzyme (Figure 1A). Similarly, ribosome binding of human NMT2 was strongly increased in the presence of NAC (Figure 1A). These results suggest that NAC physically interacts with the two closely related human NMT paralogs to facilitate their binding to the ribosome.

To quantitatively determine how NAC affects the binding affinity of NMTs to ribosomes translating N-myristoylation substrates, we purified translationally stalled ribosome-nascent chain complexes (RNCs) bearing the nascent chain of the proto-oncogene tyrosine kinase Src, a well-established NMT substrate.[14,23,24] The nascent chain contained residues 2–71 of Src and started with the 2nd glycine residue (RNC$^{Src\text{-}G}$), the neo-N terminus after initiator methionine excision by METAP1 (Figure S1A). Binding of NMT1 to RNC$^{Src\text{-}G}$ was measured using Förster resonance energy transfer (FRET) between a donor dye site specifically incorporated in the Src nascent chain and an acceptor dye on NMT1 (Figure S1; see STAR Methods). Equilibrium titrations showed high-affinity binding of NMT1 to RNC$^{Src\text{-}G}$ in the presence of NAC, with an equilibrium dissociation constant (K_d) of 0.63 nM, whereas NMT1 binding was over 20-fold weaker in the absence of NAC (Figure 1B).

These *in vitro* observations suggest that NAC provides key interactions to enable high-affinity binding for NMTs on ribosomes to facilitate N-myristoylation of nascent proteins in cells. Consistent with such a role, knockdown of NAC strongly reduced the ribosome association of NMT1 and NMT2 in human cells (Figures 1C and S1D). Moreover, the N-myristoylation of a Src-related model substrate (Src exon 1 fused to GFP; Figures S1E and S1F) was strongly reduced in NAC-depleted cells (Figure 1D). Therefore, in addition to METAP1 and NatA,[20,21] NAC also recruits NMTs to translating ribosomes to ensure the efficient cotranslational N-myristoylation of proteins in cells.

Ribosome interaction mechanism of human NMTs

To understand how NMTs are positioned on ribosomes and cotranslationally engage their substrates, we determined the structure of NMT1 and NAC bound to RNC$^{Src\text{-}G}$ by single-particle cryo-electron microscopy (cryo-EM) to an overall resolution of 2.8 Å. The cryo-EM map showed the stalled translating ribosome with NAC and NMT1 bound at the exit region of the nascent polypeptide tunnel (Figures 2A and S2). NAC and NMT1 were solved

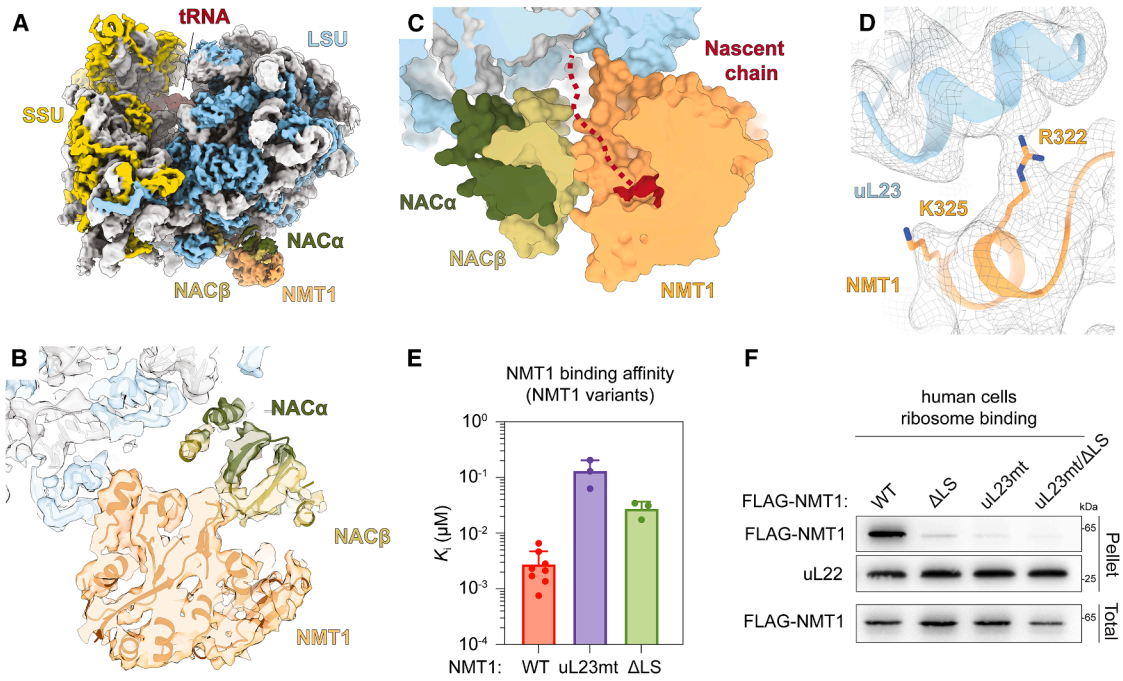

Figure 2. Cryo-EM map of RNC$^{Src\text{-}G}$ in complex with NAC and NMT1

(A) Overview of the cryo-EM map of RNC$^{Src\text{-}G}$ (65 aa) in the ternary complex with NMT1 and NAC.

(B) Cross-section of the ribosomal tunnel exit. The map was lowpass filtered to 5 Å.

(C) Potential path of the nascent chain from the ribosomal tunnel exit to the catalytic center of NMT1 (red dashed line). Residues that comprise the catalytic center of NMT1 are colored red.

(D) Close-up view of the interaction region between NMT1 and the ribosomal protein uL23. Key interacting residues are shown as sticks and the high-resolution map as gray mesh.

(E) Binding affinity of WT NMT1 and NMT1 ribosome binding mutants (R323A/K325A, uL23mt; Δ55–65, ΔLS) to RNC$^{Src\text{-}G}$ in the presence of NAC, measured using the inhibition assay (Figure S4A). Data are shown as mean ± SD, and the dots show the values from individual replicates.

(F) Ribosome association of indicated FLAG-tagged NMT1 variants in human HEK293T cells. Proteins in total and ribosomal pellet fractions were detected by immunoblotting.

See also Figures S2, S3, and S4 and Table S2.

to local resolutions of 5–9 Å, enabling us to confidently dock known structures of NAC and NMT1 (Figures 2B and S2). The N terminus of NACβ, which acts as a high-affinity ribosomal anchor,[25] was located at the same position at eL19 and eL22 as in previous structures (Figure S3A). The globular domain of NAC was positioned next to the tunnel exit but bound at a different angle than previously observed. Compared with the canonical position observed when NAC binds alone or in complex with METAP1 or NatA,[20,21] the globular domain was tilted by ~22° (Figure S3A).

The tilted NAC conformation was likely triggered by NMT1, which bound to the ribosome at a location that would sterically clash with the globular domain of NAC in its canonical position (Figure S3A). The central domain of NMT1 contacts the ribosome directly and orients its catalytic center toward the exit of the ribosomal tunnel, where nascent protein chains emerge (Figure 2C). The primary contact between NMT1 and the ribosome was mediated by a helix-helix interaction with ribosomal protein uL23 at the tunnel exit (Figure 2D). The cryo-EM map showed well-ordered density for this region, allowing building of the atomic model of the contact region and identification of key residues (R322 and K325) that mediate the interaction. These residues are evolutionarily conserved in metazoans and are also present in human NMT2 (Figure S3B). Structure-guided mutations in NMT1 designed to disrupt this interaction (R322A/K325A, referred to as NMT1 uL23mt) weakened the binding affinity of NMT1 to RNC$^{Src\text{-}G}$ over 60-fold *in vitro* (Figures 2E and S4A) and strongly decreased the ribosome association of NMT1 in cells (Figure 2F). These data suggest that uL23 serves as a functional docking site for NMTs at the tunnel exit in metazoans.

The cryo-EM reconstruction did not resolve the ~100 amino acid long flexible N-terminal domain of NMT1, which has been reported to be involved in ribosome binding of the enzyme.[26,27] The N-terminal region of NMTs is overall poorly conserved in metazoans, except for a distinct poly-lysine segment found in vertebrates (Figure S3B). Deletion of this motif (Δ55–65, referred to as NMT1 ΔLS) weakened NMT1 binding affinity for RNC$^{Src\text{-}G}$ ~10-fold *in vitro* (Figures 2E and S4A) and reduced the ribosome association of NMT1 in human cells (Figure 2F). The interaction of NMT1 ΔLS with ribosomes was also reduced in the absence of NAC (Figure S4D). Thus, vertebrate NMTs appear to make two independent ribosome contacts: a flexible interaction via the N-terminal domain that likely ensures high local concentration of the enzyme in the vicinity of the ribosome, and a positional

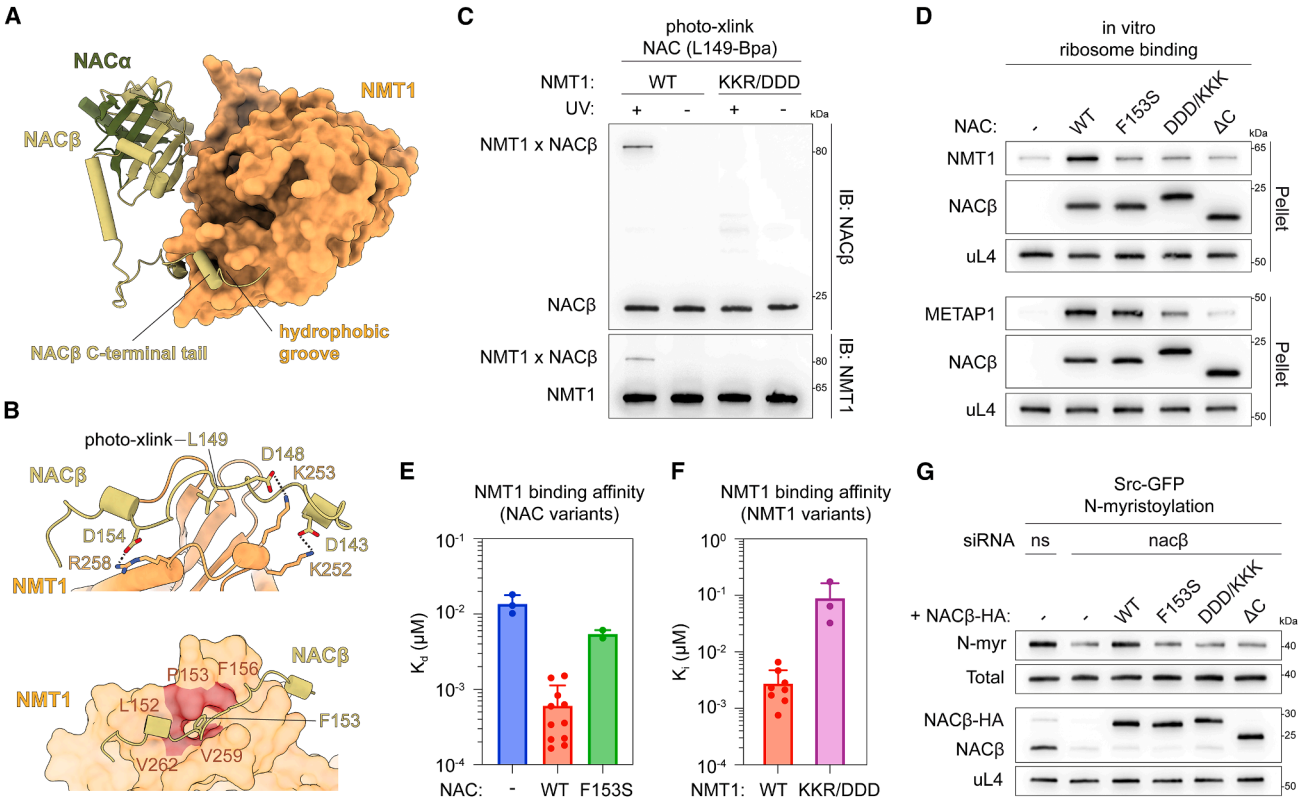

Figure 3. NMT1 is recruited by the flexible C-terminal tail of NACβ

(A) AlphaFold2 model predicts an interaction of the NACβ C-terminal tail with a hydrophobic groove on NMT1.

(B) Close-up of AlphaFold2-predicted NACβ-NMT1 binding interface. Predicted salt bridges (upper) and hydrophobic interactions (lower) are indicated. NMT1 residues forming a hydrophobic pocket for NACβ F153 are colored red. NACβ L149 served as incorporation site of a photo-crosslinking amino acid for analysis in (C).

(C) Photo-crosslinking of NAC containing the UV-activated crosslinking amino acid benzoyl-phenylalanine (Bpa) at position L149 with WT NMT1 and an NMT1 variant carrying charge reversal mutations (K252D/K253D/R258D, KKR/DDD) in predicted NACβ binding interface shown in (B). Proteins were detected by immunoblotting (IB).

(D) Ribosome binding of NMT1 (upper) and METAP1 (lower) in presence of NAC variants carrying mutations in NACβ C-terminal tail indicated in (B). Ribosomal pellet fractions were analyzed by immunoblotting. D143K/D148K/D154K, DDD/KKK; Δ140–162, ΔC.

(E) Binding affinity of WT NMT1 to $RNC^{Src\text{-}G}$ bound to the indicated NAC variants, measured using the FRET assay. Data are shown as mean ± SD, and the dots show the K_d values from independent titrations. The −NAC and WT data are from Figure 1B and are shown for comparison.

(F) Binding affinity of WT and mutant NMT1 K252D/K253D/R258D (KKR/DDD) for $RNC^{Src\text{-}G}$ bound to WT NAC, measured using the inhibition assay (Figure S4A). Data are shown as mean ± SD, and the dots show the K_i values from independent titrations. The WT data are from Figure 2E and are shown for comparison.

(G) N-myristoylation of NMT model substrate (Src N terminus fused to GFP) in human cells expressing indicated NACβ variants. Protein levels were detected by immunoblotting.

See also Figures S4 and S5.

contact at uL23 that stabilizes and positions the catalytic domain at the ribosomal tunnel exit.

NMT1 is recruited by the flexible C-terminal arm of NACβ

The two central globular domains of NAC and NMT1 were bound to the ribosome very close to each other but did not appear to make direct contact. This seemed surprising considering the strong stabilizing effect of NAC on NMT1 ribosome binding observed *in vitro* and in cells. However, at lower contour levels of the cryo-EM map, a density could be seen protruding from the NAC globular domain toward a hydrophobic groove located on the central domain of NMT1 (Figure S5A). We hypothesized that this density might correspond to one of the flexible tails of NAC that were previously shown to recruit other cotranslational protein biogenesis factors.[20,21,25] We therefore used AlphaFold2[28] to predict the structural basis of this potential NAC-NMT1 interaction.

Consistent with our hypothesis, AlphaFold2 predicted an interaction between the NMT1 central domain and the unstructured C-terminal tail of NACβ (Figures 3A and S5A), the same flexible tail of NAC that binds METAP1.[20] The predicted interaction is mediated by a conserved hydrophobic motif located within a negatively charged region near the C terminus of NACβ that binds in a hydrophobic groove on NMT1 flanked by positively charged residues (Figures 3B and S3C). The hydrophobic and basic residues in NMT1 predicted to interact with NACβ are highly conserved in eukaryotes and are also present in human NMT2

(Figure S3B). The predicted NMT1 interaction motif of NACβ partially overlaps with that of METAP1 but also includes NMT1-specific contacts such as NACβ F153 (Figure S5B).

To test the AlphaFold2 model, we designed mutations in NACβ as well as NMT1. Charge reversal mutations were introduced either in NMT1 (KKR/DDD) or in NACβ (DDD/KKK) to disrupt the predicted salt bridges between the NMT1 residues K252, K253, and R258 and NACβ residues D143, D148, and D154 (Figure 3B). To disrupt the predicted hydrophobic interaction, a point mutation was introduced in NACβ at position F153 (substituted to serine, F153S). This residue was predicted to slip into a pocket formed by conserved hydrophobic residues of NMT1, including L152, P153, F156, V259, and V262 (Figures 3B, S3B, and S5B). NMT1 variants harboring mutations at this pocket were unstable and could therefore not be investigated. Additionally, we constructed a deletion mutant lacking the entire C terminus of NACβ (Δ140–162, referred to as NACβ ΔC).

The binding of the NACβ C-terminal tail to the groove on NMT1 was then tested using a NAC variant carrying a photo-crosslinking probe at position L149 of NACβ, located in the predicted NMT1 binding motif (Figure 3B). This variant crosslinked strongly with wild-type (WT) NMT1 but not with the NMT1 KKR/DDD variant (Figure 3C). Reverse crosslinking with an NMT1 variant carrying Bpa in the hydrophobic groove at position F156 (Figure 3B) led to the same results (Figure S5C). Thus, the NACβ C terminus indeed appears to bind NMT1 in the surface patch predicted by AlphaFold2. We then investigated the importance of the NACβ tail interaction for ribosome binding of NMT1. All mutations designed to disrupt the NACβ-NMT1 interaction (NMT1 KKR/DDD and NACβ F153S, DDD/KKK, ΔC) almost completely abolished the stabilizing effect of NAC on ribosome binding of NMT1 (Figure 3D). Similar results were obtained with human NMT2 (Figure S5D).

When we investigated the impact of these mutations in NAC on ribosome binding of METAP1, we observed weaker binding for NACβ DDD/KKK and ΔC but not for the NACβ F153S mutation (Figure 3D). These results are consistent with the partially overlapping binding region of the NACβ tail interacting with both METAP1 and NMT1, while a key interaction mediated via the evolutionarily conserved F153 appears to be specific for interaction with NMTs (Figure S5B). Consistently, quantitative FRET-based measurements showed a significantly weaker binding affinity of NMT1 to RNC$^{Src\text{-}G}$ in the presence of the F153S-NAC variant, similar to that observed in the absence of NAC (Figures 3E and S4B). Reciprocally, mutations on the NMT1 surface that prevent its interaction with the NACβ tail (KKR/DDD) reduced the binding affinity of the enzyme to RNC$^{Src\text{-}G}$ more than ~30-fold, comparable to the affinity observed without NAC (Figures 3F and S4A). Consistent with these data, ribosome binding of NMT1 KKR/DDD was also severely impaired in cells, similar to when the enzyme's direct ribosome contacts were disrupted (Figure S5E).

These data suggest that the NACβ C terminus provides key binding affinity for NMTs on ribosomes. We therefore tested the importance of this interaction for N-myristoylation of proteins in human cells. We found that N-myristoylation of the Src-based reporter in NACβ knockdown cells could be efficiently restored by WT NACβ, whereas the NACβ mutants, including the F153S variant that does not affect METAP1 binding, showed no rescue effect (Figure 3G). Thus, the interaction of the flexible C-terminal NACβ arm with NMTs is critical for N-myristoylation of nascent proteins in cells.

Interplay of NMT1 with METAP1

N-myristoylation of nascent proteins requires well-coordinated binding of NMTs to translating ribosomes. NMTs must engage their substrates after methionine cleavage by METAP1 but before NatA to prevent the potential acetylation of the neo-N-terminal glycine residue by this competing enzyme.[8] This raises the question of how NAC orchestrates the binding of these three enzymes in the correct order to ensure efficient and specific N-terminal modification of nascent chains.

Both METAP1 and NMT1 are recruited by the same arm of NAC (NACβ C terminus[20]), and their binding on the surface of the ribosome next to uL23 at the tunnel exit overlaps significantly (Figure 4A). This suggests that the two enzymes cannot bind to ribosomes simultaneously. In line with this, *in vitro* binding studies showed that the two enzymes can displace each other from the ribosome (Figure 4B). Therefore, a controlled exchange of METAP1 for NMT1 must take place after methionine cleavage to enable N-myristoylation of the nascent chain.

We hypothesized that this enzyme exchange could be triggered by the nature of the N terminus of the nascent protein before and after the excision of initiator methionine. We therefore measured the affinity of NMT1 to NAC-bound RNCs containing residues 1–71 of Src so that the nascent chain starts with the first methionine residue (RNC$^{Src\text{-}M}$). Strikingly, the affinity of NMT1 to RNC$^{Src\text{-}M}$ was almost ~100-fold weaker compared with RNC$^{Src\text{-}G}$ (Figures 4C and S4C). Similarly, we observed a strong decrease in binding affinity upon mutation of the Src N-terminal N-myristoylation motif (^{2}GSNKSK^{7} to ^{2}SVNKVE,^{7} RNC$^{Src\text{-}mut}$) and with RNCs translating a NatA substrate (^{2}SACARPL^{8} and RNC^{uL4}) (Figures 4C and S4C). This suggests that the N-terminal sequence of a nascent NMT substrate contributes importantly to the binding affinity of the enzyme to the translating ribosome after methionine excision. The strong and specific binding can be explained by the confined substrate recognition pocket of NMTs, which accommodates N-terminal peptide stretches (8–9 aa) with specific consensus sequences (GxxxS+).[11] Consistent with this, an active site NMT inhibitor that binds in the peptide-binding pocket[29] strongly diminished the ribosome association of NMT1 in cell lysates translating RNC$^{Src\text{-}G}$ (Figure S5F). Likewise, an N-terminal methionine would sterically hinder the binding of the substrate sequence in the binding pocket of NMTs (Figure 4D). Thus, NMT1 strongly discriminates against METAP substrates and specifically engages the neo-N terminus of the nascent protein only after the N-myristoylation motif has been unmasked by excision of the initiator methionine. This specificity enables the controlled exchange of METAP1 for NMT1 on the ribosome.

Interplay of NMT1 with NatA

It was recently shown that NAC forms a quaternary complex at the ribosomal tunnel exit together with METAP1 and NatA, which ensures methionine excision and subsequent N-acetylation of

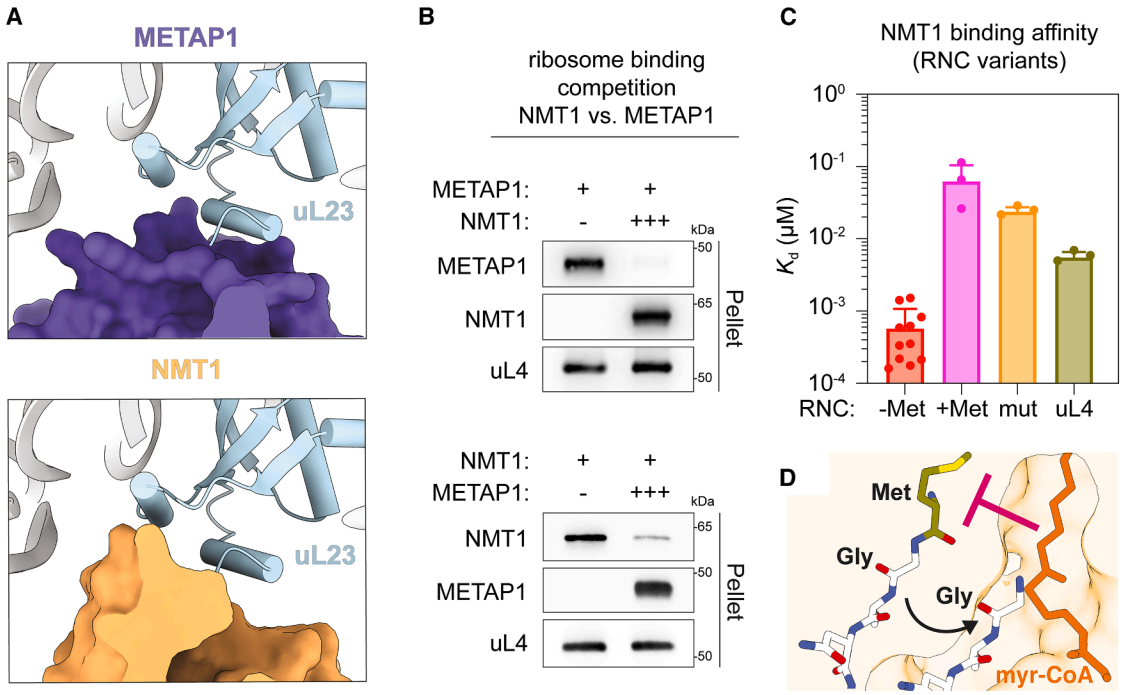

Figure 4. NMT1 exchanges with METAP1 on RNCs after methionine cleavage

(A) Surface representations of METAP1 and NMT1 docked to the ribosomal tunnel exit around uL23.

(B) Ribosome binding of METAP1 (upper) and NMT1 (lower) in presence and absence of excess NMT1 and METAP1, respectively. Ribosomal pellet fractions were analyzed by immunoblotting.

(C) Binding affinity of WT NMT1 for the indicated RNC^{Src} nascent chain variants and RNC^{uL4} (a NatA substrate) in the presence of WT NAC. Data are shown as mean ± SD, and the dots show the K_d value from independent titrations. The −Met data are from the WT data from Figure 1B and are shown for comparison.

(D) N-terminal Src peptide with terminal glycine residue modeled into NMT1 active site based on crystal structure PDB: 6qrm. The Src peptide with N-terminal methionine (left) does not fit into the substrate binding pocket due to collision with the interior of the NMT1 pocket and myristoyl-Coenzyme A (myr-CoA).

See also Figure S4.

the nascent chain N terminus.[21] The two enzymes are recruited by different tails of NAC and therefore likely bind to the ribosome simultaneously. This indicates that, initially, not only METAP1 but also NatA may bind next to the tunnel exit during the translation of N-myristoylation substrates in cells. This raises the question of whether the exchange of METAP1 for NMT1 after methionine excision may influence NatA binding, particularly considering that NMT1 induces a tilt of the NAC globular domain (Figure S3A).

We therefore used cryo-EM to investigate the structure of $RNC^{Src\text{-}G}$ in complex with NAC, NMT1, and NatA. The reconstruction with an overall resolution of 3.4 Å showed the stalled translating ribosome with NAC, NMT1, and NatA bound at the polypeptide tunnel exit on the large ribosomal subunit (Figures 5A and S6). NAC, NMT1, and NatA were solved to local resolutions of 6–10 Å, enabling us to confidently dock known structures of these factors (Figures 5B and S6). The position of NAC and NMT1 was the same as in the ternary complex described above, including the observed tilt of the NAC globular domain. NatA was bound to $RNC^{Src\text{-}G}$ at the same location and via the same interactions as in a previously observed complex together with NAC and METAP1 bound to an RNC translating a NatA substrate (RNC^{uL4}), including interaction of the C-terminal ubiquitin-associated domain (UBA) of NACα that mediates high-affinity NatA recruitment and the NACα helix (H2) that mediates the catalytic activation of NatA (Figures 5B and 5C).[21] This suggests that despite the tilt of the NAC globular domain in the presence of NMT1, NatA could bind to the ribosome in an active conformation.[21] Consistent with this, we found that cotranslational N-acetylation of a NatA model substrate (SNAP25) by NatA was not affected *in vitro* by the presence of high concentrations of NMT1 (Figure S5G). Similarly, strong overexpression of NMT1 in human cells did not affect the N-acetylation of a NatA model substrate (Figure S5H). Therefore, recruited by NAC, NatA and NMT1 can simultaneously bind to translating ribosomes in an active state.

The strong and sequence-specific interaction of NMT1 with $RNC^{Src\text{-}G}$ with the 70 aa long nascent chain (Figure 4C) indicates that the neo-N terminus of a nascent NMT substrate is tightly bound by the enzyme at an early stage of translation. These results are consistent with the distance between the active site of NMT1 and the ribosomal exit tunnel, which is comparable to that of METAP1 (~50 Å, Figure 5D), suggesting that N-myristoylation can occur immediately after methionine excision (at nascent chain length of ~60–70 aa).[20,21] On the other hand, the active site of NatA is positioned ~60 Å from the ribosome tunnel exit (Figure 5D), and efficient N-terminal acetylation was observed only when the nascent chain exceeded ~100 aa in length.[21]

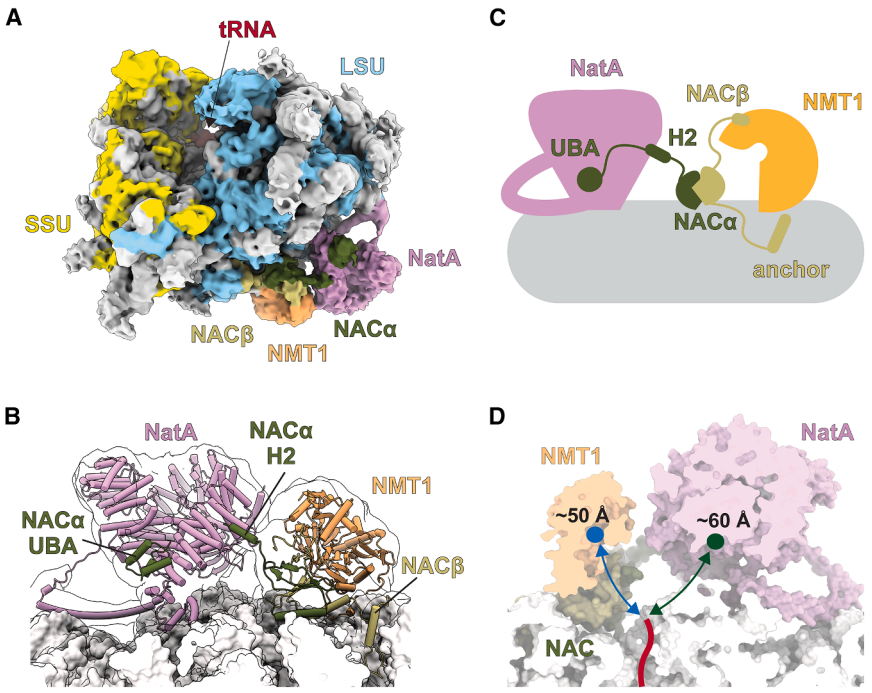

Figure 5. NMT1 and NatA can dock simultaneously to translating ribosomes

(A) Overview of the cryo-EM map of RNC$^{Src\text{-}G}$ in the quaternary complex with NAC, NMT1, and NatA. The map was lowpass filtered to 8 Å.

(B) Close-up view of the ribosomal tunnel exit. Ribosome is shown as surface, and NAC, NMT1, and NatA as cartoon. The outline shows the cryo-EM map lowpass filtered to 8 Å.

(C) Schematic representation of the quaternary complex.

(D) Cross-section of the quaternary complex to show positions of the active sites of the enzymes (blue circle, NMT1; green circle, NatA) relative to the ribosomal tunnel exit. Red line indicates nascent chain inside the ribosomal tunnel.

See also Figures S5 and S6 and Table S2.

Based on a translation elongation rate of ~5 aa/s,[30] these observations suggest that NMT1 can engage the N terminus of a nascent chain ~6 s before NatA. The time window available to NMT1 and its remarkably high affinity and specificity for methionine-excised NMT recognition motifs likely allow N-myristoylation of nascent proteins to proceed unaffected even when NatA is docked to the same ribosome in an active state. The simultaneous docking of NatA and NMT1 could also explain why some proteins containing weaker N-myristoylation motifs display both modifications in cells.[8,22]

DISCUSSION

Based on our results, we propose a mechanistic model for how NAC coordinates the binding of NMT, METAP1, and NatA to the ribosome to enable efficient cotranslational N-myristoylation of proteins in cells (Figure 6). NAC is highly abundant and binds to virtually all translating ribosomes in the cytosol through its NACβ anchor and the central globular domain.[2] As the nascent chain emerges from the ribosomal tunnel, NAC initially forms a methionine excision complex with METAP1. This enzyme is recruited by the C-terminal arm of NACβ and directly docks to the NAC globular domain in its canonical position.[20] NMT binding is disfavored at this stage due to its low affinity for nascent chains that still contain the initiator methionine, even when an N-myristoylation substrate is being translated. However, NatA can bind on the opposite side of the NAC globular domain and is recruited via the UBA domain in the flexible C-terminal arm of NACα. As previously shown, this quaternary ribosomal METAP1-NAC-NatA complex ensures the efficient N-acetylation of most methionine-cleaved substrates (>40% of the cytosolic proteome).[21] However, when methionine is cleaved from a nascent protein with a consensus N-terminal myristoylation motif, METAP1 is rapidly exchanged for NMT. This exchange is selectively triggered by a strong increase in the affinity of NMT toward the processed N-terminal motif in the nascent chain and facilitated by the interaction with the NACβ C terminus and the ribosome. In the active complex, NMT stably docks to the binding site at the exit of the ribosomal tunnel, leading to the slight tilt of the NAC globular domain as observed in this study. Despite the conformational change of NAC, NatA can remain bound to the ribosome in an active state, which explains how a subset of proteins can be both acetylated and myristoylated in cells.[8,22]

The identified ribosome binding mechanism of human NMT1 and its cooperation with NAC are likely to be largely conserved in metazoans. Vertebrates appear to have evolved an additional flexible N-terminal ribosomal anchor in NMTs that tethers the enzyme in the vicinity of the ribosome. This contact and interaction with the flexible NACβ C-terminal tail likely keep the enzyme near the ribosomal tunnel exit and thus promote a timely exchange of METAP1 for NMT immediately after methionine excision. In addition to the N-terminal modification enzymes (NMT1, NMT2, METAP1, and NatA), NAC has also been shown to regulate the cotranslational binding of the endoplasmic reticulum targeting factor SRP and the chaperone CHP1 using its two flexible C-terminal tails.[25,31] These tails of NAC thus appear to fulfill a more general function by increasing the local concentration of various protein biogenesis factors in the vicinity of the ribosomal tunnel exit to ensure rapid scanning and timely processing of nascent proteins by their appropriate factors. The globular domain of NAC, on the other hand, fulfills a regulatory role and controls the access of cotranslational factors to the ribosome tunnel exit in a nascent chain-specific manner.[20,21,25] Together, these mechanisms improve the efficiency and specificity of cotranslational protein biogenesis processes in eukaryotes.

N-myristoylation of proteins by NMTs plays a crucial process in several biological pathways found to be deregulated in cancer. For instance, the well-established proto-oncogene kinases Src and Abl require the lipid modification to efficiently transmit their growth signals.[32,33] In cell culture and mouse models, NMT inhibitors were found to be very potent in killing a wide range of

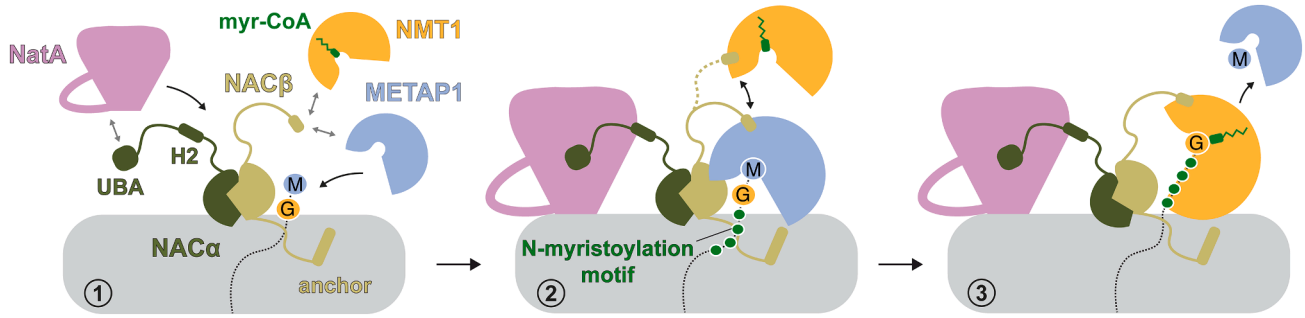

Figure 6. Mechanistic model of cotranslational N-myristoylation

NAC increases the local concentration of METAP1, NatA, and NMT1 near the ribosomal tunnel exit using its flexible C-terminal tails (1). METAP1 binds along with NatA to the tunnel exit and cleaves the initiator methionine of the nascent chain (2). Methionine excision unmasks the N-myristoylation signal in the nascent chain, leading to rapid exchange of METAP1 for NMT1 at the tunnel exit. NMT1 then myristoylates the N-terminal glycine residue in the nascent chain (3).

different cancer cells.[34–36] Recently, a first in-human trial was started with the NMT inhibitor zelenirstat for the treatment of B-cell lymphoma.[16] NMT inhibitors were also shown to be effective against viral infections. Many viruses that infect humans, including HIV, SARS-CoV-2, and Mpox virus, require the activity of the host NMTs for efficient replication.[18,37] Moreover, inhibitors targeting NMTs of protozoan parasites are currently being developed to treat diseases such as malaria, leishmaniasis, and African sleeping sickness.[38–40] The NMT inhibitors, which are currently entering early stages of clinical development, all target the catalytic center of the enzyme. The identified hydrophobic groove on NMTs, where the C-terminal tail of NACβ binds, could be a promising new druggable site. Targeting this binding site could be a means to selectively inhibit the cotranslational function of NMTs while sparing their described posttranslational activity.[14] Such selective inhibitors could potentially avoid the cellular toxicity associated with active site inhibition.

Limitations of the study

Protein synthesis in cells is a dynamic process in which 3–6 new amino acids are added to the nascent polypeptide chain every second. However, several experiments carried out in this study rely on artificially stalled RNCs. Although this system has reliably recapitulated many aspects of cotranslational protein biogenesis processes previously, we cannot exclude the possibility that the enzymes function differently to some extent during ongoing translation. In addition, many molecular interactions could affect the optimal positioning of the enzyme at the ribosome that is crucial for catalysis, and these effects may not be fully captured in binding measurements. Furthermore, in cells, several other cotranslational factors compete for access to the ribosomal tunnel exit. These factors could affect the binding mode of the enzymes and complexes investigated in this study and thus subtly alter the proposed mechanistic model.

RESOURCE AVAILABILITY

Lead contact

Further information and requests for resources and reagents should be directed to the lead contact, Elke Deuerling (elke.deuerling@uni-konstanz.de).

Materials availability

Plasmids described in this paper are available from the lead contact upon reasonable request.

Data and code availability

- The models and cryo-EM maps generated in this study were deposited at the PDB and EMDB under IDC codes PDB: 9QQA, EMD: 53295 (Ternary complex of translating ribosome, NAC, and NMT1) and PDB: 9QQB, EMD: 53296 (quaternary complex of translation ribosome, NAC, NMT1, and NatA).
- This paper does not report original code.
- Any additional information required to reanalyze the data reported in this paper is available from the lead contact upon request.

ACKNOWLEDGMENTS

We thank R. Schloemer and G. Hunaeus for technical assistance. This work was supported by the German Science Foundation (SFB969/A07) to E.D. and M.G., German Science Foundation grant 537004599 to E.D. and M.G., the Swiss National Science Foundation (SNSF grant 310030_212308 to N. Ban), the National Center of Excellence in Research RNA & Disease Program of the SNSF (grant 51NF40-205601 to N. Ban), the European Research Council (Synergy Grant 101072047 CoTransComplex to N. Ban), and the National Institute of Health grant R35 GM136321 to S.-o.S. We thank the ETH Scientific Center for Optical and Electron Microscopy (ScopeM) for technical support.

AUTHOR CONTRIBUTIONS

Conceptualization, M.G., N. Ban, S.-o.S., and E.D.; investigation: M.G., N. Burg, and S.P. performed cell and *in vitro* biochemical experiments; B.E., M. J., and A.S. prepared the cryo-EM samples and processed the cryo-EM data; and A.M.L. and Z.F. performed FRET affinity measurements and *in vitro* NatA activity assays; writing – original draft, M.G. and B.E.; writing – review & editing, N. Ban, S.S., A.M.L., M.J., and E.D.; supervision, S.-o.S., N. Ban, E.D., and M.G.; funding acquisition, S.-o.S., N. Ban, E.D., and M.G.

DECLARATION OF INTERESTS

The authors declare no competing interests.

STAR★METHODS

Detailed methods are provided in the online version of this paper and include the following:

- KEY RESOURCES TABLE
- EXPERIMENTAL MODEL AND STUDY PARTICIPANT DETAILS

SUPPLEMENTAL INFORMATION

Supplemental information can be found online at https://doi.org/10.1016/j.molcel.2025.06.015.

Received: January 6, 2025
Revised: May 13, 2025
Accepted: June 17, 2025
Published: July 9, 2025

REFERENCES

1. Deng, S., and Marmorstein, R. (2021). Protein N-Terminal Acetylation: Structural Basis, Mechanism, Versatility, and Regulation. Trends Biochem. Sci. *46*, 15–27. https://doi.org/10.1016/j.tibs.2020.08.005.
2. Gamerdinger, M., and Deuerling, E. (2024). Cotranslational sorting and processing of newly synthesized proteins in eukaryotes. Trends Biochem. Sci. *49*, 105–118. https://doi.org/10.1016/j.tibs.2023.10.003.
3. Giglione, C., Fieulaine, S., and Meinnel, T. (2015). N-terminal protein modifications: Bringing back into play the ribosome. Biochimie *114*, 134–146. https://doi.org/10.1016/j.biochi.2014.11.008.
4. Aksnes, H., Drazic, A., Marie, M., and Arnesen, T. (2016). First Things First: Vital Protein Marks by N-Terminal Acetyltransferases. Trends Biochem. Sci. *41*, 746–760. https://doi.org/10.1016/j.tibs.2016.07.005.
5. Wilcox, C., Hu, J.S., and Olson, E.N. (1987). Acylation of proteins with myristic acid occurs cotranslationally. Science *238*, 1275–1278. https://doi.org/10.1126/science.3685978.
6. Starheim, K.K., Gevaert, K., and Arnesen, T. (2012). Protein N-terminal acetyltransferases: when the start matters. Trends Biochem. Sci. *37*, 152–161. https://doi.org/10.1016/j.tibs.2012.02.003.
7. Xiao, Q., Zhang, F., Nacev, B.A., Liu, J.O., and Pei, D. (2010). Protein N-terminal processing: substrate specificity of Escherichia coli and human methionine aminopeptidases. Biochemistry *49*, 5588–5599. https://doi.org/10.1021/bi1005464.
8. Castrec, B., Dian, C., Ciccone, S., Ebert, C.L., Bienvenut, W.V., Le Caer, J.P., Steyaert, J.M., Giglione, C., and Meinnel, T. (2018). Structural and genomic decoding of human and plant myristoylomes reveals a definitive recognition pattern. Nat. Chem. Biol. *14*, 671–679. https://doi.org/10.1038/s41589-018-0077-5.
9. Meinnel, T., Dian, C., and Giglione, C. (2020). Myristoylation, an Ancient Protein Modification Mirroring Eukaryogenesis and Evolution. Trends Biochem. Sci. *45*, 619–632. https://doi.org/10.1016/j.tibs.2020.03.007.
10. Giglione, C., and Meinnel, T. (2022). Mapping the myristoylome through a complete understanding of protein myristoylation biochemistry. Prog. Lipid Res. *85*, 101139. https://doi.org/10.1016/j.plipres.2021.101139.
11. Dian, C., Pérez-Dorado, I., Rivière, F., Asensio, T., Legrand, P., Ritzefeld, M., Shen, M., Cota, E., Meinnel, T., Tate, E.W., et al. (2020). High-resolution snapshots of human N-myristoyltransferase in action illuminate a mechanism promoting N-terminal Lys and Gly myristoylation. Nat. Commun. *11*, 1132. https://doi.org/10.1038/s41467-020-14847-3.
12. Kosciuk, T., Price, I.R., Zhang, X., Zhu, C., Johnson, K.N., Zhang, S., Halaby, S.L., Komaniecki, G.P., Yang, M., DeHart, C.J., et al. (2020). NMT1 and NMT2 are lysine myristoyltransferases regulating the ARF6 GTPase cycle. Nat. Commun. *11*, 1067. https://doi.org/10.1038/s41467-020-14893-x.
13. Su, D., Kosciuk, T., Yang, M., Price, I.R., and Lin, H. (2021). Binding Affinity Determines Substrate Specificity and Enables Discovery of Substrates for N-Myristoyltransferases. ACS Catal. *11*, 14877–14883. https://doi.org/10.1021/acscatal.1c03330.
14. Thinon, E., Serwa, R.A., Broncel, M., Brannigan, J.A., Brassat, U., Wright, M.H., Heal, W.P., Wilkinson, A.J., Mann, D.J., and Tate, E.W. (2014). Global profiling of co- and post-translationally N-myristoylated proteomes in human cells. Nat. Commun. *5*, 4919. https://doi.org/10.1038/ncomms5919.
15. Beauchamp, E., Yap, M.C., Iyer, A., Perinpanayagam, M.A., Gamma, J.M., Vincent, K.M., Lakshmanan, M., Raju, A., Tergaonkar, V., Tan, S.Y., et al. (2020). Targeting N-myristoylation for therapy of B-cell lymphomas. Nat. Commun. *11*, 5348. https://doi.org/10.1038/s41467-020-18998-1.
16. Sangha, R., Jamal, R., Spratlin, J., Kuruvilla, J., Sehn, L.H., Beauchamp, E., Weickert, M., Berthiaume, L.G., and Mackey, J.R. (2024). A first-in-human phase I trial of daily oral zelenirstat, a N-myristoyltransferase inhibitor, in patients with advanced solid tumors and relapsed/refractory B-cell lymphomas. Investig. New Drugs *42*, 386–393. https://doi.org/10.1007/s10637-024-01448-w.
17. Tate, E.W., Soday, L., de la Lastra, A.L., Wang, M., and Lin, H. (2024). Protein lipidation in cancer: mechanisms, dysregulation and emerging drug targets. Nat. Rev. Cancer *24*, 240–260. https://doi.org/10.1038/s41568-024-00666-x.
18. Priyamvada, L., Kallemeijn, W.W., Faronato, M., Wilkins, K., Goldsmith, C.S., Cotter, C.A., Ojeda, S., Solari, R., Moss, B., Tate, E.W., et al. (2022). Inhibition of vaccinia virus L1 N-myristoylation by the host N-myristoyltransferase inhibitor IMP-1088 generates non-infectious virions defective in cell entry. PLOS Pathog. *18*, e1010662. https://doi.org/10.1371/journal.ppat.1010662.
19. Frearson, J.A., Brand, S., McElroy, S.P., Cleghorn, L.A.T., Smid, O., Stojanovski, L., Price, H.P., Guther, M.L.S., Torrie, L.S., Robinson, D.A., et al. (2010). N-myristoyltransferase inhibitors as new leads to treat sleeping sickness. Nature *464*, 728–732. https://doi.org/10.1038/nature08893.
20. Gamerdinger, M., Jia, M., Schloemer, R., Rabl, L., Jaskolowski, M., Khakzar, K.M., Ulusoy, Z., Wallisch, A., Jomaa, A., Hunaeus, G., et al. (2023). NAC controls cotranslational N-terminal methionine excision in eukaryotes. Science *380*, 1238–1243. https://doi.org/10.1126/science.adg3297.
21. Lentzsch, A.M., Yudin, D., Gamerdinger, M., Chandrasekar, S., Rabl, L., Scaiola, A., Deuerling, E., Ban, N., and Shan, S.O. (2024). NAC guides a ribosomal multienzyme complex for nascent protein processing. Nature *633*, 718–724. https://doi.org/10.1038/s41586-024-07846-7.
22. Utsumi, T., Sato, M., Nakano, K., Takemura, D., Iwata, H., and Ishisaka, R. (2001). Amino acid residue penultimate to the amino-terminal gly residue strongly affects two cotranslational protein modifications, N-myristoylation and N-acetylation. J. Biol. Chem. *276*, 10505–10513. https://doi.org/10.1074/jbc.M006134200.
23. Ishizawar, R., and Parsons, S.J. (2004). c-Src and cooperating partners in human cancer. Cancer Cell *6*, 209–214. https://doi.org/10.1016/j.ccr.2004.09.001.
24. Schultz, A.M., Henderson, L.E., Oroszlan, S., Garber, E.A., and Hanafusa, H. (1985). Amino terminal myristylation of the protein kinase p60src, a

retroviral transforming protein. Science *227*, 427–429. https://doi.org/10.1126/science.3917576.

25. Jomaa, A., Gamerdinger, M., Hsieh, H.H., Wallisch, A., Chandrasekaran, V., Ulusoy, Z., Scaiola, A., Hegde, R.S., Shan, S.O., Ban, N., et al. (2022). Mechanism of signal sequence handover from NAC to SRP on ribosomes during ER-protein targeting. Science *375*, 839–844. https://doi.org/10.1126/science.abl6459.
26. Glover, C.J., Hartman, K.D., and Felsted, R.L. (1997). Human N-myristoyltransferase amino-terminal domain involved in targeting the enzyme to the ribosomal subcellular fraction. J. Biol. Chem. *272*, 28680–28689. https://doi.org/10.1074/jbc.272.45.28680.
27. Giang, D.K., and Cravatt, B.F. (1998). A second mammalian N-myristoyltransferase. J. Biol. Chem. *273*, 6595–6598. https://doi.org/10.1074/jbc.273.12.6595.
28. Jumper, J., Evans, R., Pritzel, A., Green, T., Figurnov, M., Ronneberger, O., Tunyasuvunakool, K., Bates, R., Žídek, A., Potapenko, A., et al. (2021). Highly accurate protein structure prediction with AlphaFold. Nature *596*, 583–589. https://doi.org/10.1038/s41586-021-03819-2.
29. Spassov, D.S., Atanasova, M., and Doytchinova, I. (2023). Inhibitor Trapping in N-Myristoyltransferases as a Mechanism for Drug Potency. Int. J. Mol. Sci. *24*, 11610. https://doi.org/10.3390/ijms241411610.
30. Gerashchenko, M.V., Peterfi, Z., Yim, S.H., and Gladyshev, V.N. (2021). Translation elongation rate varies among organs and decreases with age. Nucleic Acids Res. *49*, e9. https://doi.org/10.1093/nar/gkaa1103.
31. Minoia, M., Quintana-Cordero, J., Jetzinger, K., Kotan, I.E., Turnbull, K.J., Ciccarelli, M., Masser, A.E., Liebers, D., Gouarin, E., Czech, M., et al. (2024). Chp1 is a dedicated chaperone at the ribosome that safeguards eEF1A biogenesis. Nat. Commun. *15*, 1382. https://doi.org/10.1038/s41467-024-45645-w.
32. Hantschel, O., Nagar, B., Guettler, S., Kretzschmar, J., Dorey, K., Kuriyan, J., and Superti-Furga, G. (2003). A myristoyl/phosphotyrosine switch regulates c-Abl. Cell *112*, 845–857. https://doi.org/10.1016/s0092-8674(03)00191-0.
33. Patwardhan, P., and Resh, M.D. (2010). Myristoylation and membrane binding regulate c-Src stability and kinase activity. Mol. Cell. Biol. *30*, 4094–4107. https://doi.org/10.1128/MCB.00246-10.
34. Geroyska, S., Mejia, I., Chan, A.A., Navarrete, M., Pandey, V., Kharpatin, S., Noguti, J., Wang, F., Srole, D., Chou, T.F., et al. (2024). N-Myristoytransferase Inhibition Causes Mitochondrial Iron Overload and Parthanatos in TIM17A-Dependent Aggressive Lung Carcinoma. Cancer Res Commun. *4*, 1815–1833. https://doi.org/10.1158/2767-9764.CRC-23-0428.
35. Chen, Y.C., Navarrete, M.S., Wang, Y., McClintock, N.C., Sakurai, R., Wang, F., Chen, K.T., Chou, T.F., Rehan, V.K., Lee, D.J., et al. (2020). N-myristoyltransferase-1 is necessary for lysosomal degradation and mTORC1 activation in cancer cells. Sci. Rep. *10*, 11952. https://doi.org/10.1038/s41598-020-68615-w.
36. Thinon, E., Morales-Sanfrutos, J., Mann, D.J., and Tate, E.W. (2016). N-Myristoyltransferase Inhibition Induces ER-Stress, Cell Cycle Arrest, and Apoptosis in Cancer Cells. ACS Chem. Biol. *11*, 2165–2176. https://doi.org/10.1021/acschembio.6b00371.
37. Rivière, F., Dian, C., Dutheil, R.F., Monassa, P., Giglione, C., and Meinnel, T. (2024). Novel, tightly structurally related N-myristoyltransferase inhibitors display equally potent yet distinct inhibitory mechanisms. Structure *32*, 1737–1750.e3. https://doi.org/10.1016/j.str.2024.08.001.
38. Rodríguez-Hernández, D., Vijayan, K., Zigweid, R., Fenwick, M.K., Sankaran, B., Roobsoong, W., Sattabongkot, J., Glennon, E.K.K., Myler, P.J., Sunnerhagen, P., et al. (2023). Identification of potent and selective N-myristoyltransferase inhibitors of Plasmodium vivax liver stage hypnozoites and schizonts. Nat. Commun. *14*, 5408. https://doi.org/10.1038/s41467-023-41119-7.
39. Corpas-Lopez, V., Moniz, S., Thomas, M., Wall, R.J., Torrie, L.S., Zander-Dinse, D., Tinti, M., Brand, S., Stojanovski, L., Manthri, S., et al. (2019). Pharmacological Validation of N-Myristoyltransferase as a Drug Target in Leishmania donovani. ACS Infect. Dis. *5*, 111–122. https://doi.org/10.1021/acsinfecdis.8b00226.
40. Nascimento, I.J.D.S., Cavalcanti, M.A.T., and de Moura, R.O. (2023). Exploring N-myristoyltransferase as a promising drug target against parasitic neglected tropical diseases. Eur. J. Med. Chem. *258*, 115550. https://doi.org/10.1016/j.ejmech.2023.115550.
41. Yin, J., Lin, A.J., Golan, D.E., and Walsh, C.T. (2006). Site-specific protein labeling by Sfp phosphopantetheinyl transferase. Nat. Protoc. *1*, 280–285. https://doi.org/10.1038/nprot.2006.43.
42. Hsieh, H.H., Lee, J.H., Chandrasekar, S., and Shan, S.O. (2020). A ribosome-associated chaperone enables substrate triage in a cotranslational protein targeting complex. Nat. Commun. *11*, 5840. https://doi.org/10.1038/s41467-020-19548-5.
43. Punjani, A., Rubinstein, J.L., Fleet, D.J., and Brubaker, M.A. (2017). cryoSPARC: algorithms for rapid unsupervised cryo-EM structure determination. Nat. Methods *14*, 290–296. https://doi.org/10.1038/nmeth.4169.
44. Pettersen, E.F., Goddard, T.D., Huang, C.C., Meng, E.C., Couch, G.S., Croll, T.I., Morris, J.H., and Ferrin, T.E. (2021). UCSF ChimeraX: Structure visualization for researchers, educators, and developers. Protein Sci. *30*, 70–82. https://doi.org/10.1002/pro.3943.
45. Goddard, T.D., Huang, C.C., Meng, E.C., Pettersen, E.F., Couch, G.S., Morris, J.H., and Ferrin, T.E. (2018). UCSF ChimeraX: Meeting modern challenges in visualization and analysis. Protein Sci. *27*, 14–25. https://doi.org/10.1002/pro.3235.
46. Emsley, P., Lohkamp, B., Scott, W.G., and Cowtan, K. (2010). Features and development of Coot. Acta Crystallogr. D Biol. Crystallogr. *66*, 486–501. https://doi.org/10.1107/S0907444910007493.
47. Adams, P.D., Afonine, P.V., Bunkóczi, G., Chen, V.B., Davis, I.W., Echols, N., Headd, J.J., Hung, L.W., Kapral, G.J., Grosse-Kunstleve, R.W., et al. (2010). PHENIX: a comprehensive Python-based system for macromolecular structure solution. Acta Crystallogr. D Biol. Crystallogr. *66*, 213–221. https://doi.org/10.1107/S0907444909052925.
48. Gamerdinger, M., Kobayashi, K., Wallisch, A., Kreft, S.G., Sailer, C., Schlömer, R., Sachs, N., Jomaa, A., Stengel, F., Ban, N., et al. (2019). Early Scanning of Nascent Polypeptides inside the Ribosomal Tunnel by NAC. Mol. Cell *75*, 996–1006.e8. https://doi.org/10.1016/j.molcel.2019.06.030.
49. Sharma, A., Mariappan, M., Appathurai, S., and Hegde, R.S. (2010). In vitro dissection of protein translocation into the mammalian endoplasmic reticulum. Methods Mol. Biol. *619*, 339–363. https://doi.org/10.1007/978-1-60327-412-8_20.
50. Connell, E., Darios, F., Peak-Chew, S., Soloviev, M., and Davletov, B. (2009). N-terminal acetylation of the neuronal protein SNAP-25 is revealed by the SMI81 monoclonal antibody. Biochemistry *48*, 9582–9589. https://doi.org/10.1021/bi9012403.
51. Evans, R., O'Neill, M., Pritzel, A., Antropova, N., Senior, A., Green, T., Žídek, A., Bates, R., Blackwell, S., Yim, J., et al. (2022). Protein complex prediction with AlphaFold-Multimer. Preprint at bioRxiv. https://doi.org/10.1101/2021.10.04.463034.
52. Mizushima, S., and Nagata, S. (1990). pEF-BOS, a powerful mammalian expression vector. Nucleic Acids Res. *18*, 5322. https://doi.org/10.1093/nar/18.17.5322.
53. Liebschner, D., Afonine, P.V., Baker, M.L., Bunkóczi, G., Chen, V.B., Croll, T.I., Hintze, B., Hung, L.W., Jain, S., McCoy, A.J., et al. (2019). Macromolecular structure determination using X-rays, neutrons and electrons: recent developments in Phenix. Acta Crystallogr. D Struct. Biol. *75*, 861–877. https://doi.org/10.1107/S2059798319011471.

STAR★METHODS

KEY RESOURCES TABLE

REAGENT or RESOURCE	SOURCE	IDENTIFIER
Antibodies		
Anti-FLAG (ms)	Merck	Cat# F1804; RRID:AB_262044
Anti-MetAP1 (ms)	Bethyl Laboratories	Cat# A305-584A; RRID:AB_2891500
Anti-NMT1 (ms)	Santa Cruz	Cat# sc-393702
Anti-NACB (rb)	Abcam	Cat# ab203517; RRID:AB_2783867
Anti-NMT1 (rb)	Biorbyt	Cat# 11546-1-AP; RRID:AB_2153157
Anti-NMT2 (ms)	Santa Cruz	Cat# sc-136005; RRID:AB_2153300
Anti-SNAP25 (ms)	Biolegend	Cat# 836304; RRID:AB_2566521
Anti-uL22 (ms)	Santa Cruz	Cat# sc-515904; RRID:AB_3107048
Anti-uL4 (ms)	Santa Cruz	Cat# sc-100838; RRID:AB_2181910
Anti-GFP (ms)	Roche	Cat# 11814460001; RRID:AB_390913
Anti-uL16 (ms)	Abcepta	Cat# AP19053a
HRP-anti-mouse IgG (secondary)	Jackson	Cat# 715-035-151; RRID:AB_2340771
HRP-anti-rabbit IgG (secondary)	Jackson	Cat# 711-035-152; RRID:AB_10015282
Bacterial and virus strains		
E. coli BL21 (DE3)	Merck	Cat# 69450-3
E. coli BL21 (DE3) Rosetta	Merck	Cat# 70954
E. coli DH5α	Thermo Fisher	Cat# 18265017
Chemicals, peptides, and recombinant proteins		
14-Azido-myristic acid	Iris	Cat# RL-3230.0100
Biotin-PEG4-alkyne	Merck	Cat# 764213-5MG
Complete EDTA-free protease inhibitor cocktail	Roche	Cat# 5056489001
DNase I	Merck	Cat# DN25
DTT (1,4-Dithiothreit)	Carl Roth	Cat# 6908.4
GFP-Trap® magnetic agarose	Chromotek	Cat# gtma
Human MetAP1	Gamerdinger et al.[20]	N/A
Human NACA-NACB-D143K_D148K_D154K (DDD/KKK)	This study	N/A
Human NACA-NACB ΔC	Gamerdinger et al.[20]	N/A
Human NACA-NACB-Bpa L149	This study	N/A
Human NACA-NACB F153S	This study	N/A
Human NMT1	This study	N/A
Human NMT1-ΔK55-65 (ΔLS)	This study	N/A
Human NMT1-Bpa F156	This study	N/A
Human NMT1-K252D_K253D_R258D (KKR/DDD)	This study	N/A
Human NMT1-R322A_325A (uL23mt)	This study	N/A
Human NMT1-R322A_325A_ΔK55-65 (uL23mt/ΔLS)	This study	N/A
Human NMT1-yBBR 103	This study	N/A
Human NMT2	This study	N/A
IPTG (Isopropyl β-D-1-thiogalactopyranoside)	Roth	Cat# CN08.3
Ni-IDA matrix, Protino	Macherey-Nagel	Cat# 745210.30
para-benzoylphenylalanine (Bpa)	Bachem	Cat# 4017646.005

(*Continued on next page*)

Continued

REAGENT or RESOURCE	SOURCE	IDENTIFIER
Streptavidin-HRP conjugate	Merck	Cat# GERPN1231
Ulp1 peptidase	This study	N/A
Critical commercial assays		
Click-&-Go™ Click Chemistry Reaction Buffer Kit	Vector laboratories	Cat# CLK-CSTM
SFP enzyme	Yin et al.[41]	N/A
trans-Cyclooct-2-en – L – Lysine (TCOK)	Sichem	Cat# SC-8008
PylRS	Hsieh et al.[42]	N/A
Pyl tRNA	Hsieh et al.[42]	N/A
NAC	Lentzsch et al.[21]	N/A
Atto647N-maleimide	ATTO-TEC	Cat# AD 647N-41
Cy3B Tetrazine	AAT Bioquest	Cat# ABD-948
NatA	Lentzsch et al.[21]	N/A
HYPK	Lentzsch et al.[21]	N/A
NMT1 inhibitor IMP-366 (DDD85646)	Cayman	Cat# 1215010-55-1
Deposited data		
Cryo-EM density map of Ternary complex of translating ribosome, NAC and NMT1	This study	EMDB: EMD-53295
Cryo-EM density map of Quaternary complex of translating ribosome, NAC, NMT1 and NatA	This study	EMDB: EMD-53296
Atomic model of the Ternary complex of translating ribosome, NAC and NMT1	This study	PDB: 9QQA
Atomic model of the Quaternary complex of translating ribosome, NAC, NMT1 and NatA	This study	PDB: 9QQB
Experimental models: Cell lines		
HEK293T	ATCC	RRID: CVCL_0063
Oligonucleotides		
siNACB-as (3′UTR) 5′-AAU AGC AGC UCC CAG UAA C-dTdT-3′	Biomers	N/A
siNACB-s (3′UTR) 5′-GUU ACU GGG AGC UGC UAU U-dTdT-3′	Biomers	N/A
siNMT1-as (3′UTR) 5′-AUU UUC AGU GGC UUU AUC C-dTdT-3′	Biomers	N/A
siNMT1-s (3′UTR) 5′-GGA UAA AGC CAC UGA AAA U-dTdT-3′	Biomers	N/A
siNMT2-as (3′UTR) 5′-AAU UUC ACU UGA GUU GUG C-dTdT-3′	Biomers	N/A
siNMT2-s (3′UTR) 5′-GCA CAAC UCA AGU GAA AUU-dTdT-3′	Biomers	N/A
siNS-as 5′-ACG UGA CAC GUU CGG AGA A-dTdT-3′	Biomers	N/A
siNS-s 5′-UUC UCC GAA CGU GUC ACG U-dTdT-3′	Biomers	N/A
Recombinant DNA		
p3xFLAG-NMT1-ΔK+uL23mt+KKR/DDD	This study	N/A
p3xFLAG-NMT1-ΔK55-65 (ΔLS)	This study	N/A
p3xFLAG-NMT1-K252D_K253D_R258D (KKR/DDD)	This study	N/A
p3xFLAG-NMT1-R258D	This study	N/A

(*Continued on next page*)

Continued

REAGENT or RESOURCE	SOURCE	IDENTIFIER
p3xFLAG-NMT1-R322A_325A_ΔK55-65 (uL23mt/LS)	This study	N/A
p3xFLAG-NMT1-R323A/K325A (uL23mt)	This study	N/A
p3xFLAG-NMT1-WT	This study	N/A
p3xHA-NACB D143K_D148K_D154K (DDD/KKK)	This study	N/A
p3xHA-NACB F153S	This study	N/A
p3xHA-NACB-ΔC	Gamerdinger et al.[20]	N/A
p3xHA-NACB-WT	Gamerdinger et al.[20]	N/A
Src-Exon1-EGFP-FLAG (Src-GFP)	This study	N/A
pSOS5133 Src RNC 70aa amber @aa28 – iMet	This study	N/A
pSOS5136 Src RNC 100aa amber @aa60 – iMet	This study	N/A
pSOS5153 Src RNC 70aa amber @aa28 + iMet	This study	N/A
pSOS5158 Src RNC 70aa amber @aa28 mutant	This study	N/A
pSOS5120 His_SUMO_NMT1_human_yBBR_103	This study	N/A
pSOS5220 His-SUMO-NMT1_human Delta K (55–65 deletion) with Ybbr 103	This study	N/A
pSOS5221 His-SUMO-NMT1_human UL23 MT R322A,K325A with Ybbr 103	This study	N/A
pSOS5223 His-SUMO-NMT1_human K252D, K253D, R258D with Ybbr 103	This study	N/A
pSOS4828 IRES-3xFLAG-SUMO-SMI epitope-uL4	Lentzsch et al.[21]	N/A
pSOS5573 IRES-3XFLAG-SUMO-M1S Rpl4 Amber 27	This study	N/A
Software and algorithms		
FelixFL	HORIBA	v1.0.34.0
EPU	Thermo Fisher Scientific	https://www.thermofisher.com/us/en/home/electronmicroscopy/products/software-em-3d-vis/epusoftware.html
CryoSPARC	Punjani et al.[43]	https://cryosparc.com/
USF Chimera	Pettersen et al.[44]	https://www.cgl.ucsf.edu/chimera/download.html
UCSF ChimeraX	Goddard et al.[45]	https://www.cgl.ucsf.edu/chimerax/
Coot 0.9.8.5	Emsley et al.[46]	https://www2.mrc-lmb.cam.ac.uk/personal/pemsley/coot/
Phenix	Adams et al.[47]	https://www.phenix-online.org/
Other		
DMEM (Dulbecco's Modified Eagle Medium)	Gibco	Cat# 41966-029
Opti-MEM® (Reduced Serum Medium)	Gibco	Cat# 31985-070
FBS	Bio&SELL	Cat# FBS.S.0615

EXPERIMENTAL MODEL AND STUDY PARTICIPANT DETAILS

HEK293T cells (RRID: CVCL_0063) were from ATCC. The cell line was frequently checked for proper morphology under the microscope but was not authenticated. Cell line was negative for mycoplasma throughout all experiments. Cells were cultured in

Dulbecco's Modified Eagle's Medium (DMEM) supplemented with 10% fetal calf serum (FCS) and 100 μg/ml Normocin in a 5% CO_2 atmosphere at 37°C. Sex of cell line is female.

METHOD DETAILS

Protein purifications

Human NAC (NACα/NACA + NACβ/BTF3b complex) and METAP1 were recombinantly expressed in E. coli BL21(DE3) and purified as previously described.[21,25,48] NatA (NAA10+NAA15 complex), and HYPK were purified as recently described.[21] For NatA, 6xHis-NAA15 and NAA10 were co-expressed from a bicistronic plasmid in BYC123 yeast cells. Cells were lysed by cryo-milling and protein was purified using Ni-sepharose HP (Cytiva), followed by chromatography on a MonoS cation exchange column (Cytiva). For HYPK, 6xHis-SUMO-HYPK isoform 2 was expressed in BL21(DE3) cells. HYPK in clarified cell lysate was purified by Ni-Sepharose HP (Cytiva) chromatography, followed by cleavage of the His-tag using Ulp1 protease and chromatography over a MonoQ anion exchange column (Cytiva). Fractions containing purified protein were pooled and frozen in aliquots using liquid nitrogen and stored at -80°C.

Human NMT1 and NMT2 (wildtype and mutants) were expressed as a His-SUMO fusion protein in E. coli BL21(DE3) cells. Cells were cultured at 37°C to an OD600 of 1.5, then shifted to 20°C, and expression was induced with 1 mM IPTG for 3 hours. Cells were resuspended in lysis buffer (50 mM Na-PO_4 pH 8.0, 300 mM NaCl, 6 mM $MgCl_2$, 2 mM β-mercaptoethanol, 10 % Glycerol, 8 μg/ml Pepstatin, 10 μg/ml Aprotinin, 5 μg/ml Leupeptin, 2 mM AEBSF) followed by addition 5 mg DNase I. Cells were extracted using a high-pressure homogenizer (Avestin EmulsiFlex C3) and the lysate cleared by centrifugation (two times for 20 min, 16.000 rpm, 4°C). His affinity purification was performed using a gravity column with Ni-IDA matrix (Protino; Macherey-Nagel). The column was washed with lysis buffer containing 750 mM NaCl until absorption at 280 nm reached the baseline. Protein was then eluted with elution buffer (lysis buffer containing 250 mM Imidazole) and dialyzed (20 mM Na-PO_4 pH 7.4, 25 mM NaCl, 6 mM $MgCl_2$, 2 mM β-mercaptoethanol, 5% Glycerol) overnight in the presence of SUMO protease (Ulp1, 8 μg/mg protein). NMT protein was then purified by cation exchange chromatography using a MonoS 5/50 column (Cytiva). Fractions containing NMT protein were pooled, dialyzed overnight in storage buffer (20 mM Na-PO_4 pH 7.4, 25 mM NaCl, 6 mM $MgCl_2$, 2 mM β-mercaptoethanol, 10% Glycerol), frozen in liquid N_2, and stored at -80°C.

Human NAC and NMT1 carrying the photo-crosslinking amino acid p-Benzoylphenylalanine (Bpa, Bachem) at specific positions were recombinantly expressed and purified as previously described.[25,48]

RNC^{Src} purification and labeling for affinity measurements

mRNA transcripts for the translation reaction were generated as follows. Dpn1 treated and purified PCR amplicons encoding IRES-3xFLAG-SUMO-Src(2-71) were used as templates for *in vitro* transcription using the Megascript T7 protocol. Its mRNA was precipitated with an equal volume of 8M $LiCl_2$ at -30°C overnight and was pelleted by centrifugation at 4°C at 14k RPM for 30min. The RNA pellet was washed with ice cold 70% ethanol, dried and redissolved in 100 μL H_2O at a concentration of 3-4 μg/μL.

In vitro translation was conducted at 32°C for 30 min in a 10 mL reaction containing 0.01 g/L mRNA, 1x T2 mix (for details see Lentzsch et al.[21] and Sharma et al.[49]), 1.5 mM $MgCl_2$, 50 mM KCl, 0.3 mM spermidine, 5 mM DTT, 40 μM methionine, 1x protease inhibitor (GoldBio) and an amber suppression system consisting of 1 μM PylRS, 0.1 g/L Pyl tRNA, and 0.1 mM trans-Cyclooct-2-en–L-Lysine.[42]

Following translation, the reaction was supplemented with 15 mM $Mg(OAc)_2$, 666 mM KOAc, and 0.1% Triton X-100 (Sigma), layered over a 10 mL sucrose cushion containing 50 mM HEPES-KOH, pH 7.5, 1 M KOAc, 15 mM $Mg(OAc)_2$, 0.5 M sucrose, 0.1% Triton X-100), and centrifuged at 58k RPM for 2 h at 4 °C in a Ti70 rotor (Beckman Coulter). Ribosome pellet was resuspended in 1 mL Equilibration Buffer (50 mM HEPES-KOH, pH 7.5, 100 mM KOAc, 2 mM $Mg(OAc)_2$) and rotated for 15 min at 25 °C. Aggregates were removed by centrifugation at 4 °C for 5 min at 14k RPM. The supernatant was transferred to a fresh amber tube and incubated with 1 μM Cy3B-tetrazine dye conjugate (final concentration) for 20 min with rotation at 25 °C in the dark. The reaction was added to 333 μL of equilibrated Anti-DYKDDDDK Magnetic Agarose (Pierce), and binding was conducted at 20 min at 25 °C with rotation followed by 40 min at 4 °C with rotation. The beads were spun down for 2 min at 1000 xg and washed 3 times with Wash Buffer 1 (50 mM HEPES-KOH, pH 7.5, 300 mM KOAc, 2 mM $Mg(OAc)_2$) and 3 times with Wash Buffer 2 (50 mM KHEPES-KOH, pH 7.5, 100 mM KOAc, 0.1% Triton X-100, 2 mM $Mg(OAc)_2$), each for 10 min with rotation at 4 °C. Washed resin was re-equilibrated 3 times with 1 mL of Equilibration Buffer. RNC was eluted with 666 μL Elution Buffer (50 mM HEPES-KOH, pH 7.5, 100 mM KOAc, 2 mM $Mg(OAc)_2$ and 1.5 mg/mL 3xFLAG peptide (Apex Bio. SKU: A6001-25)) for 1 hour at 4°C and a second time with 333 μL Elution Buffer for 15 min at 4°C. The 3xFLAG-SUMO tag of the RNC was cleaved with Ulp1 (25 μg/mL) for 1h at 4 °C. This mixture was layered over a 2 mL 0.5 M sucrose cushion in RNC Buffer (50 mM HEPES-KOH, pH 7.5, 150 mM KOAc, 5 mM $Mg(OAc)_2$) and centrifuged in a TLA 100.3 rotor at 100k RPM for 1h at 4°C. The ribosome pellet was resuspended in RNC buffer supplemented with 1 mM DTT and 0.02% octaethylene glycol monododecyl ether (Sigma) at a final concentration of 200-400 nM. Single use aliquots were frozen in liquid nitrogen and stored at -80°C. Fluorescently labelled RNC^{uL4} (70 aa) were generated as previously described.[21]

Purification and fluorescent labeling of NMT1 for affinity measurements

For FRET measurements, human NMT1 was expressed as a N-terminally SUMO-fused protein (6xHis-SUMO-NMT1) in Rosetta BL21 (DE3) cells. 2 L of cells were grown at 37°C to an OD_{600} of 0.66, when expression was induced with 1 mM isopropyl β-D-1-thiogalactopyranoside (IPTG) and temperature was reduced to 25°C. Cells were harvested 16 h later and frozen at -80°C. For protein purification, the pellet was thawed and resuspended in 30 mL of B1 buffer (50 mM $NaPO_4$, pH 8.0, 300 mM NaCl, 6 mM $MgCl_2$, 2 mM β-mercaptoethanol, 10% glycerol, 1 mM AEBSF, 1x protease inhibitor cocktail (GoldBio)). The resuspended cell paste was lysed by sonication and clarified by centrifugation for 1 h at 16k RPM and 4°C in a JA20 rotor (Beckman Coulter). Clarified lysate was mixed with 2 mL Ni-NTA (Goldbio) resin preequilibrated in B1 buffer and incubated for 30 min with rotation at 4°C. The slurry was transferred to a column, and the resin was washed with 75 CV B2 buffer (B1 buffer with 750 mM NaCl without protease inhibitors) and 25 CV B3 buffer (B1 buffer with 25 mM NaCl without protease inhibitors). Protein was eluted with 4 CV B4 buffer (B1 plus 250 mM imidazole) with rotation in batch for 15min at 4°C. Ulp1 protease (homemade) was added to the eluant at 10 μg/mL to cleave 6xHis-SUMO, and the eluant was dialyzed overnight into B5 buffer with 25 mM NaCl (20 mM $NaPO_4$, pH 7.4, 6 mM $MgCl_2$, 2 mM β-mercaptoethanol, 5% glycerol) using 3.5 MW SnakeSkin Dialysis Tubing (ThermoFisher). Dialyzed protein was loaded onto a 1 mL HiTrap SP HP cation exchange chromatography column (Cytiva) at 0.5 ml/min, washed at 1 ml/min with B5 buffer with 25 mM NaCl and eluted at 0.5 ml/min with a 25 CV linear gradient of 25 mM to 650 mM NaCl in Buffer B5. Peak fractions were then concentrated using a 10K MW cutoff Amicon Centrifugal concentrator (Millipore Sigma) to 1 ml and purified on a Superdex 75 Increase 10/300 GL size exclusion column (Cytiva) in buffer B6 (20 mM $NaPO_4$, pH 7.4, 25 mM NaCl, 6 mM $MgCl_2$, 2 mM β-mercaptoethanol, 10% glycerol). Peak protein fractions were pooled and concentrated to 50 μM and frozen in single use aliquots in liquid nitrogen and stored in -80°C. NMT1 concentration was determined using an ε = 70,820 $M^{-1}cm^{-1}$ at 280 nm.

To label NMT1, the 11 aa ybbR motif[41] was inserted between residues 103-104. YbbR-tagged NMT1 was expressed and purified as for WT NMT1. 10 μM ybbR-NMT1 in Buffer B5 with 25 mM NaCl was fluorescently labeled in a 1 ml reaction containing 20 μM Atto647N-CoA dye conjugate, 2.5 μM SFP enzyme (homemade[41]) for 1 h at 25°C in the dark. The reaction mixture was centrifuged at 14k RPM for 15 min at 4°C, and supernatant was purified on Superdex 75 Increase 10/300 GL size exclusion column (Cytiva) in buffer B6. The peak NMT1 fractions were concentrated with a 10kd cutoff Amicon Centrifugal concentrator (Millipore Sigma) and frozen in single use aliquots in liquid nitrogen at -80°C. The concentration of labeled NMT1 was determined using Equation 1:

$$NMT1\ concentration\ (M) = \frac{A_{280} - (A_{646} \times CF)}{\varepsilon} \quad \text{(Equation 1)}$$

where A_{280} is the absorbance of the purified protein at 280 nm, A_{646} is the peak absorbance of dye, CF is the correction factor at 280 nm for Atto647N dye (0.04), and ε = 70,820 $M^{-1}cm^{-1}$ at 280 nm for NMT1. The concentration of Atto647N was determined using ε_{646} = 150,000 $M^{-1}cm^{-1}$. Protein labeling efficiency was calculated as the ratio of the concentrations of Atto647N to NMT1 in the sample.

FRET measurements

Prior to all biochemical measurements, the proteins were centrifuged at 100k RPM for 30 min in a TLA 100 rotor (Beckman coulter). All fluorescent measurements were obtained on a FluoroQM-75-22 spectrofluorometer (HORIBA) with a PMT detector at 25°C in SRP buffer supplemented with 1 mg/ml BSA to reduce nonspecific binding.

Fluorescence emission spectra were acquired from 550 – 720 nm using an excitation wavelength of 535 nm. When indicated, reactions contained 2 nM $RNC^{Src\text{-}G}$-Cy3B, 10 nM NMT1-Atto647N, and 50 nM NAC.

Equilibrium titrations were acquired using an excitation wavelength of 535 nm and emission wavelength of 577 nm, with 2 sec integration time. Reactions contained 2 nM $RNC^{Src\text{-}G}$-Cy3B and NMT1-Atto647N at the indicated concentrations. As a control for environmental effects or fluorescence artifacts, titrations with unlabeled NMT1 were performed in parallel. After correcting for dilution, observed FRET efficiency (E) was calculated using Equation 2:

$$E = 1 - \frac{F_{DA}}{F_D} \quad \text{(Equation 2)}$$

where F_{DA} and F_D are the fluorescence intensity in the presence and absence of NMT1-Atto647N, respectively. The NMT1 concentration dependence of E was fit to Equation 3:

$$E = E_{Max} \times \frac{K_d + [RNC]_0 + [NMT1] - \sqrt{\left(K_d + [RNC]_0 + [NMT1]\right)^2 - 4[RNC]_0[NMT1]}}{2[RNC]_0} \quad \text{(Equation 3)}$$

in which E_{Max} is the maximum FRET efficiency at saturating NMT1 concentrations, K_d is the equilibrium dissociation constant (K_d) between NMT1 and RNC.

For competition experiments, increasing concentrations of unlabeled WT or mutant NMT1 (I) was added to a solution containing 2 nM $RNC^{Src\text{-}G}$-Cy3B and 30 nM NMT1-Atto647N ($NMT1^{L}$). Observed FRET efficiency was plotted as a function of I concentration and fit to Equation 4:

$$E = E_{Max} \times \frac{K_i\left(1+\frac{[NMT1^L]}{K_{d,L}}\right)}{[I]+K_i\left(1+\frac{[NMT1^L]}{K_{d,L}}\right)} \quad \text{(Equation 4)}$$

in which E_{Max} is the FRET efficiency in the absence of inhibitor, $K_{d,L}$ is the K_d of NMT1-Atto647N (set to 1 nM), and K_i is the inhibition constant for unlabeled NMT1. K_i is equal to the K_d of unlabeled NMT1 for $RNC^{Src\text{-}G}$.

In vitro N-terminal acetylation reactions

Prior to the assay, proteins were centrifuged for 30 min at 4 °C at 100k RPM in a TLA 100 rotor (Beckman Coulter) in an Optima TLX Ultracentrifuge (Beckman Coulter). RNCs were centrifuged for 5 min at 4°C at 14k RPM in a 5425 rotor (Beckman Coulter). $RNC_{SNAP25\text{-}uL4}$ bearing a model NatA substrate were generated and purified as described[21] and contained residues 2-12 of SNAP25 followed by residues 1-94 or 1-124 of uL4 in the nascent chain. The Nt-acetylated 11 residues of SNAP25 are specifically recognized by the SMI81 antibody,[50] providing a readout for N-terminal acetylation on the RNC. Reactions were carried out in RNC buffer supplemented with 5 mM DTT and 0.02% octaethylene glycol monododecyl ether (Sigma) and contained 70 nM $RNC_{SNAP25\text{-}uL4}$ (total nascent length of 105 or 135 amino acids), 100 μM acetyl-CoA (Sigma), 300 nM hNatA or hNatA-HYPK complex (formed with 1:1.2 molar ratio), 400 nM NAC, and with or without 300 nM NMT1. Reactions were initiated by the addition of acetyl-CoA. Reaction aliquots were removed at 5, 10, 60 s and quenched in 4x low pH loading dye (30% glycerol, 250 mM Bis-Tris, pH 5.7, 0.04% bromophenol blue, 8% SDS, 200 mM DTT). Reactions were analyzed by SDS-PAGE on 4-12 % Bis-Tris gels run at 200 V, followed by Western blot using primary antibodies for RpL10/uL16 rabbit (1:1,000, Abcepta, AP19053a) and SMI81 mouse (1:1,000 BioLegend, 836304). The blots were probed for 45 min with the secondary antibodies Goat anti-Rabbit (1:20,000 Licor, IRDye 680RD) and Goat anti-Mouse (1:20,000 Licor, IRDye 800CW) and the resulting bands were quantified using ImageJ v1.53t.

In vitro ribosome co-sedimentation analysis

Human ribosomes from HEK293T cells were purified as previously described.[48] Purified NAC and NMT variants were incubated with ribosomes (ribosomes 250 nM, NAC 500 nM, NMT 100 nM) for ~10 min on ice in ribosome sedimentation buffer (30 mM HEPES pH 7.4, 100 mM KOAc, 5 mM $MgCl_2$, 1x protease inhibitor cocktail (Roche)) before loading the sample on a 25% sucrose cushion prepared in the same buffer. For In the same manner NMT1-METAP1 ribosome binding competition studies were performed, except that one factor was added in 50-fold excess over the other. The ribosomes were then sedimented by ultracentrifugation (200.000 x g) for 2 hours at 4°C. Proteins in the ribosomal pellet and total fractions were then analyzed by standard SDS-PAGE and immunoblotting techniques. For the ribosome sedimentation analysis in Figure S5F non-stop mRNA encoding FLAG-SUMO-Src^{G} (70 aa) was in vitro translated in reticulocyte lysate in presence and absence of NMT inhibitor IMP-366 (50 μM) for 30 min at 26°C. After translation, lysate was placed on ice and SUMO protease (Ulp1, 100 μg/mg protein) added for 1 h. Ribosomes were then sedimented as described above except using a 40% sucrose cushion prepared in 30 mM HEPES pH 7.4, 200 mM KOAc, 5 mM $MgCl_2$. The control translation reaction lacking SUMO protease contained 2x protease inhibitor cocktail (Roche)) during translation to inhibit endogenous proteases.

In vitro photo-crosslinking

UV crosslinking of NAC and NMT1 containing Bpa at specific positions (L149 of NACβ and F156 of NMT1) was performed in a similar manner as described previously.[20] Factors were mixed in a 1:1 ratio (1.15 μM each, 17.5 μl total sample) in crosslinking buffer (20 mM HEPES pH 7.4, 100 mM NaCl, 5 mM $MgCl_2$, 5 mM DTT, 1x protease inhibitor cocktail (Roche)) and incubated on ice for ~10 min. Tubes were placed in a tight-fitting metal-rack on ice to provide intense cooling during UV irradiation. UV crosslinking was performed for 20 min at 365 nm using a Bio-Link UV crosslinker (Vilber Lourmat). Proteins were then analyzed by standard denaturing SDS-PAGE and immunoblotting techniques.

AlphaFold calculations

AlphaFold v2.2 was installed locally and used in multimer mode[51] for generating structural hypotheses for NAC-NMT1 interactions. The models were ranked according to model confidence (a weighted combination of inter-monomer and intra-monomer interaction scores) and subsequently analyzed with respect to their consistency with experimental results.

Human cell culture experiments

HEK293T cells were cultured in Dulbecco's Modified Eagle's Medium (DMEM) supplemented with 10% fetal calf serum (FCS) and 100 μg/ml Normocin in a 5% CO_2 atmosphere at 37°C. Cells were transfected with DNA and/or siRNA by electroporation in OptiMEM using a NEPA21 electroporator (Nepagene). To knockdown NACβ, cells were transiently transfected with two different

siRNAs (each 1 μg) targeting the 3'UTR of NACβ (5'-GUUACUGGGAGCUGCUAUU-dTdT-3' and 5'-GAAGCCUGGGAAU-CAAGUU-dTdT-3'). Control cells were transfected with nonsense siRNA (5'-UUCUCCGAACGUGUCACGU-dTdT-3'). NACβ expression was restored in knockdown cells by co-transfection of plasmids (20 μg) expressing C-terminally 3xHA-tagged NACβ variants from the CMV promoter and SV40 3'UTR. Cells were harvested 2 days after transfection and extracted in ice-cold lysis buffer (30 mM HEPES pH 7.4, 100 mM KOAc, 5 mM $MgCl_2$, 5% Mannitol, 0.04% octaethylene glycol monododecyl ether, 100 μg/ml Cycloheximide, 1x protease inhibitor cocktail (Roche)). Ribosomes were pelleted by ultracentrifugation (220.000 x g) through a 25% sucrose cushion (prepared in lysis buffer) for 1.5-2 hours at 4°C. Proteins in the ribosomal pellet and total fractions were then analyzed by standard SDS-PAGE and immunoblotting techniques. Ribosome binding of NMT1 mutants were analyzed by transient transfection of constructs (250 ng) encoding N-terminally 3xFLAG-tagged NMT1 variants (CMV promoter, SV40 3'UTR) in the endogenous NMT1 siRNA background. Knockdown was performed for 2 days as described for NACβ using a siRNA targeting the 3'UTR of NMT1 (5'-GGAUAAAGCCACUGAAAAU-dTdT-3').

Protein N-myristoylation was assessed by co-transfecting 10 μg of pEF-BOS vector[52] encoding human Src-exon 1 (amino acids 1-83) fused to GFP-FLAG. Cells were fed 100 nM azido-myristic acid (Iris Biotech) for 6 h (for inhibitor experiment) or 18 hours (for knockdown experiments) before harvest. Cells were extracted in reporter lysis buffer (50 mM Na-PO_4 pH 7.5, 150 mM NaCl, 2 mM EDTA, 1 mM EGTA, 0.5% NP40, 1x protease inhibitor cocktail (Roche)) and the lysate cleared by centrifugation (20.000 x g, 20 min, 4°C). The reporter protein was then immunoprecipitated using a nanobody GFP trap (ChromoTek). Lysates were adjusted to the same protein concentration and incubated with the beads for 1-2 hours on an orbital shaker at 4°C. After several washing steps with lysis buffer, proteins were eluted from the beads by denaturation (lysis buffer containing 2% SDS instead of NP40) and boiling at 99°C for 5 min. Total reporter levels were assessed by anti-GFP immunoblotting (Roche). N-myristoylated reporter levels were detected using Streptavidin-HRP (Merck) after copper-catalyzed cycloaddition of Biotin-PEG4-alkyne (Merck). Click chemistry was performed according to instructions using Click-&-Go Click Chemistry Reaction Buffer Kit (Click Chemistry Tools).

Protein N-acetylation under strong NMT1 overexpression conditions was assessed by co-transfecting 5 μg of pEF-BOS vector encoding the N-terminus of human SNAP25 (amino acids 1-12) fused to GFP plus/minus 10 μg 3xFLAG-NMT1 expression construct. Total and N-acetylated reporter levels were detected by immunoblotting as described previously[21] using anti-GFP and anti-N-acetyl-specific SNAP25 antibodies (see key resources table), respectively.

RNC purification for cryo-EM

RNCs were generated in vitro by translation of a non-stop mRNA. A plasmid encoding residues 2-65 of Src, fused to an N-terminal 3xFLAG-SUMO tag used for purification, was linearized via PCR and DNA extracted using the QIAquick PCR Purification Kit (Qiagen) according to the manufacturer's instructions. Purified DNA was transcribed in vitro using homemade T7 polymerase at 37°C for 2 h. Resulting mRNA was extracted via phenol-chloroform and lithium chloride purification, then resuspended in water. mRNA at a concentration of 1 μM was translated in 1 ml of Flexi Rabbit Reticulocyte Lysate (Promega), at 32°C for 20 min resulting in run-off RNCs. The RNCs were purified using FLAG-tag affinity chromatography. For purification, 0.3 ml of ANTI-FLAG M2 Affinity Gel (Sigma-Aldrich) was washed with buffer A (50 mM HEPES-KOH pH 7.6, 100 mM KCl, 5 mM $MgCl_2$, 1 mM TCEP) and incubated with the translation reaction (diluted to 2 ml) for 1 h at 4°C in a rotating chromatography column. Afterwards, the supernatant was removed by gravity flow. The beads were washed with 10 ml of buffer B (50 mM HEPES-KOH pH 7.6, 500 mM KCl, 5 mM $MgCl_2$, 1 mM TCEP) and 10 ml of buffer A. The RNCs were eluted in four fractions (0.5 ml each) with elution buffer (buffer A containing 0.1 mg ml^{-1} 3×FLAG peptide). For each elution, the beads were incubated with the elution buffer for 15 min to improve recovery before collecting the fraction. All fractions were pooled and the RNCs were pelleted by ultracentrifugation in a TLA-55 rotor (Beckman Coulter) at 186,000 g at 4°C for 2 h. The resulting RNC pellet was resuspended in cryo-EM buffer (50 mM HEPES-KOH pH 7.6, 100 mM KOAc, 5 mM $Mg(OAc)_2$, 1 mM TCEP). The sample was flash-frozen in liquid nitrogen and stored at –80°C for further use.

RNC complex assembly for cryo-EM studies

Purified RNCs were incubated with a 10-fold molar excess of Ulp1-SUMO protease (purified in-house) in cryo-EM buffer for 35 min at RT to cleave the 3xFLAG-SUMO tag. To remove the cleaved tag, the RNCs were pelleted by ultracentrifugation in a TLA-100 rotor (Beckman Coulter) at 380,000 g at 4°C for 2 h. The RNC pellet was resuspended in cryo-EM buffer. For assembly of the $RNC^{Src\text{-}G}$ in complex with NAC and NMT1, RNCs (100 nM final concentration) were incubated with NAC (0.5 μM) at 30°C for 10 min. To minimize aggregation, 0.02 % octaethylene glycol monododecyl ether was added to the RNCs. Simultaneously, human NMT1 (Y180A mutant showing reduced enzymatic activity[11]) was incubated with myristoyl-Coenzyme A sodium salt (Santa Cruz Biotechnology CAS 3130-72-1) in a 1:2 ratio (10 μM NMT1 Y180A, 20 μM myristoyl-Coenzyme A) at 25°C for 15 min. Resulting NMT1-myristoyl-Coenzyme A complex, at a final concentration of 1 μM, was added to the RNCs on ice and the sample was kept on ice until cryo-EM grid preparation. For assembly of the $RNC^{Src\text{-}G}$ in complex with NAC, NMT1 and NatA, RNCs (100 nM final concentration) were incubated with NAC (0.5 μM) at 30°C for 10 min. To minimize aggregation, 0.02% octaethylene glycol monododecyl ether was added to the RNCs. Human NMT1 WT at a final concentration of 1 μM was then added and incubated for 10 min at 30°C. This was followed by addition of NatA (1 μM), composed of the catalytically impaired Naa10 mutant E24Q/Y26F and the auxiliary subunit Naa15,[21] and incubation at 30°C for 7 min. The RNCs were kept on ice until cryo-EM grid preparation.

Cryo-EM grid preparation and data collection

Quantifoil R2/2 holey carbon grids were washed with ethyl acetate, coated with a continuous layer of 1 nm thick amorphous carbon produced in-house and glow-discharged for 15 s at 15 mA using PELCO easiGlow glow discharge cleaning system (Ted Pella, Inc.). Grids were mounted into Vitrobot MK IV (Thermo Fisher Scientific) with the chamber set to 4°C and 100% humidity. A 4 μl aliquot of the sample was applied to each grid and incubated for 30 s in the Vitrobot chamber. Excess sample was blotted off and the grids were plunge-frozen in a mixture of ethane and propane (1:2). Grids with varying blotting times were prepared and stored in liquid nitrogen until data collection.

Data was collected on a Titan Krios G3i transmission electron microscope (Thermo Fisher Scientific) operating at 300 kV and equipped with a BioQuantum imaging filter-mounted K3 direct electron detector (Gatan). The microscope was used with a nominal magnification of 81,000x. Energy filter slit was set to 20 e-V, the defocus was shifted between -0.7 and -2.2 μm in 0.3 μm steps. Data was collected using the EPU software (Thermo Fisher Scientific). For the RNC$^{Src\text{-}G}$ in complex with NAC and NMT1, a total of 11,424 movies were collected at a physical pixel size of 1.06 Å/pixel with the total electron dose of ~60 e-/Å.[2] For the RNC$^{Src\text{-}G}$ in complex with NAC, NMT1 and NatA, a total of 8,955 movies were collected at a physical pixel size of 1.06 Å/pixel with the total electron dose of ~60 e-/Å.[2]

Cryo-EM data processing

All data processing was performed in cryoSPARC.[43] Collected movies underwent motion correction and CTF parameter estimation. Particles were picked by template-matching to 80S rabbit ribosome templates low-pass filtered to 20 Å. Picked particles were extracted at pixel size of 3.19 Å/pix and subjected to 2D classification. Class averages that displayed ribosome-like particles were selected, 3D refined and subjected to 3D variability analysis followed by a clustering of the particles. Particles with well-resolved P-site tRNA were selected and homogeneously refined. For the RNC$^{Src\text{-}G}$ in complex with NAC and NMT1, additional 3D variabilities with a spherical mask positioned at the ribosomal exit tunnel and subsequent particle clustering were performed to sort for the presence of factors. Particles displaying NAC-NMT1 density were re-extracted at 1.06 Å/pix. The particles (87,143) were subjected to a final non-uniform refinement with per-particle defocus and per-group CTF parameters estimation, resulting in a reconstruction at 2.82 Å global resolution estimated using the FSC = 0.143 criterion (Figure S2). The NAC-NMT1 factors were resolved locally to ~5-9 Å (Figure S2). For the RNC$^{Src\text{-}G}$ in complex with NAC, NMT1 and NatA, 3D variabilities with a spherical mask positioned at the ribosomal exit tunnel were performed after 80S particle selection. Particles displaying NAC-NMT1 density (30,342 particles) were selected and homogenously refined. Further 3D variabilities with a spherical mask positioned in the NatA area were performed to select the subset of particles containing all three factors. The particles (15,709) were re-extracted at 1.06 Å/pix and subjected to a final non-uniform refinement with per-particle defocus and per-group CTF parameters estimation, resulting in a reconstruction at 3.43 Å global resolution estimated using the FSC = 0.143 criterion (Figure S6). The NAC, NMT1 and NatA factors were resolved locally to ~6-11 Å (Figure S6). Low pass filtering of maps and resolution estimations were performed in cryoSPARC.

Model building and refinement

A recently published model of the rabbit 80S ribosome (PDB 8p2k) was docked into the cryo-EM maps using UCSF ChimeraX.[44,45] In the model of the large ribosomal subunit, the nascent polypeptide was rebuilt as a polyalanine chain. The E-site tRNA chain was removed from the model. For the RNC$^{Src\text{-}G}$ in complex with NAC and NMT1, models of the NAC heterodimer (from PDB 8p2k) and NMT1 (from PDB 5mu6) were docked into the map. Residues up to 156 were removed from the NMT1 crystal structure, as well as the inhibitor and myristoyl-CoA. Tyr180 was mutated to Ala in COOT.[46] Docked models were manually adjusted in COOT to better fit the observed cryo-EM maps. For the RNC$^{Src\text{-}G}$ in complex with NAC, NMT1 and NatA, NAC and NatA models were obtained and docked from PDB 9f1b. The crystal structure of the WT NMT1 (PDB 5mu6) was also docked, with residues 1-156, inhibitor and myristoyl-CoA removed.

The assembled models were refined in real space for five cycles using PHENIX (version 1.21.2)[47,53] with the side chain rotamer and Ramachandran restraints. MolProbity was used to validate the refined model geometry (Table S2).

QUANTIFICATION AND STATISTICAL ANALYSIS

All the experiments were conducted at least three times. Binding affinity data (mean ± s.d.) were plotted and analyzed using PRISM (version 10.3.1). The details of replicates and statistical analysis are mentioned in the corresponding figure legends and summarized in Table S1.